A COMPUTATIONAL STUDY OF EXCITATION DYNAMICS ON SEMICONDUCTOR SURFACES

A Thesis Submitted to
the Graduate School of Engineering and Sciences of
İzmir Institute of Technology
in Partial Fulfillment of the Requirements for the Degree of

MASTER OF SCIENCE

in Materials Science and Engineering

by
Birnur KAYA

December 2019
İZMİR

We approve the thesis of **Birnur KAYA**

Examining Committee Members:

Prof. Dr. Hâldun SEVİNÇLİ
Department of Materials Science and Engineering, İzmir Institute of Technology

Prof. Dr. Serdar ÖZÇELİK
Department of Chemistry, İzmir Institute of Technology

Prof. Dr. A. Devrim GÜÇLÜ
Department of Physics, İzmir Institute of Technology

Assoc. Prof. Dr. Ümit AKINCI
Department of Physics, Dokuz Eylül University

Asst. Prof. Dr. Umut ADEM
Department of Materials Science and Engineering, İzmir Institute of Technology

17 December 2019

Prof. Dr. Hâldun SEVİNÇLİ
Supervisor, Department of Materials Science and Engineering,
İzmir Institute of Technology

Prof. Dr. Serdar ÖZÇELİK
Co-Supervisor, Department of Chemistry,
İzmir Institute of Technology

Prof. Dr. Hâldun SEVİNÇLİ
Head of the Department of Materials Science and Engineering

Prof. Dr. Mehtap EANES
Dean of Graduate School of Engineering and Science

ACKNOWLEDGMENTS

First and foremost, I would like to express my deepest gratitude to my thesis advisor Prof. Dr. Hâldun SEVİNÇLİ for his immense knowledge, encouragement and never-ending patience. He has guided me during my thesis and I have learned a lot of things from his helpful and valuable discussions. I would like to thank to my co-advisor Prof. Dr. Serdar ÖZÇELİK for his valuable information and inspiration with my studies.

I would like to thank the old and the new members of Computational Materials Physics Group, Burak ÖZDAMAR, Gizem KURT, Mustafa Neşet ÇINAR, Gözde ÖZBAL SARGIN, Abdülmenaf ALTINTAŞ, Koray SEVİM and Elif ÜNSAL for their insightful contributions to help me during my MSc study.

Furthermore, I am very thank to my best listener Tuğçe DEMİRTAY for her emionatiol support, being perfect friend when I was about to lose my motivation. I am thank to Gün Deniz AKKOÇ for his valuable discussions. I am also thank to Ezgi OĞUR for her friendship and the best coffee breaks.

I owe a special thanks to my love Kaan AKMAN for his unconditional love, patience and endless support. He is always there for me when I need.

Last but not least, I am deeply grateful to my parents Refiye and Recep KAYA for always supporting and encouraging me. I am very grateful to my dearest sister, Kübrânûr BOZ for her support and being my best friend in the world. They always motivated to me.

This thesis is supported by Scientific and Technological Research Council of Turkey (TÜBİTAK-115F616).

ABSTRACT

A COMPUTATIONAL STUDY OF EXCITATION DYNAMICS ON SEMICONDUCTOR SURFACES

Recent experimental studies have shown that collodial quantum dots can be produced in large quantities and their optical properties can be tailored by controlling their composition, size and surface characteristics. Motivated by these studies, this thesis is devoted to the investigation of excitation dynamics on semiconductor surfaces, which are passivated with organic molecules. First, constructing a simplified model, excitation dynamics is investigated by computing time dependent occupations of frontier molecular orbitals for various scenarios regarding the values for the energy gap between the highest occupied and the lowest unoccupied molecular orbitals (HOMO and LUMO), as well as the coupling strengths. Second, the model is enhanced to address realistic systems. Passivation of ZnS surface with oleic acid (OA) is modeled using density functional theory based tight binding (DFTB) simulations. Extracting the Hamiltonian and overlap matrices, excitation dynamics is studied for Zn rich and S rich surfaces and different coverage ratios of surfaces. The excitation dynamics is compared and contrasted against the simplified model. Characteristic features are identified and typical decay rates are calculated for various molecular configurations. In addition to these, X-Ray diffraction spectra of quaternary ZnCdSSe nanoalloys have been investigated.

ÖZET

YARI İLETKEN YÜZEYLERDE UYARILMA DİNAMİKLERİNİN HESAPLAMASAL OLARAK ÇALIŞILMASI

Son deneysel çalışmalar kolloidal kuantum noktalarının büyük miktarlarda üretilebileceğini ve optik özelliklerinin kompozisyonlarını, boyutlarını ve yüzey özelliklerini kontrol ederek uyarlanabileceğini göstermiştir. Bu çalışmaların motive ettiği bu tez, organik moleküllerle pasife edilmiş yarı iletken yüzeylerdeki uyarılma dinamiklerini araştırmaya adanmıştır. İlk olarak, basitleştirilmiş bir modelin oluşturulmasıyla uyarılma dinamikleri, etkileşim gücünün yanı sıra, en yüksek dolu ve en düşük boş moleküler orbitaller (HOMO ve LUMO) arasındaki enerji boşluğu değerlerine ilişkin çeşitli senaryolar için öncü moleküler orbitallerin zamana bağlı doluluk oranları hesaplanarak incelenmiştir. İkinci olarak, bu model gerçekçi sistemleri ele almak için geliştirilmiştir. ZnS yüzeyinin oleik asit (OA) ile pasive edilmesi yoğunluk fonksiyoneli teorisine dayanan sıkı bağlanma simülasyonları kullanılarak modellenmiştir. Hamiltonyen ve örtüşme matrisleri elde edilerek Zn ve S bakımından zengin yüzeylerde ve yüzeylerin farklı kaplama oranlarında uyarılma dinamikleri incelenmiştir. Uyarılma dinamikleri basitleştirilmiş modelle karşılaştırılmıştır. Karakteristik özellikler tanımlanmış ve çeşitli moleküler konfigürasyonlar için tipik bozulma oranları hesaplanmıştır. Bunlara ek olarak, kuaterner ZnCdSSe nano alaşımlarının X-ışını kırınım spektrumları incelenmiştir.

TABLE OF CONTENTS

LIST OF FIGURES

Figure **Page**

Figure **Page**

Figure **Page**

LIST OF TABLES

LIST OF ABBREVIATIONS

QD . . . . . Quantum Dot
DOS . . . . . Density of States
DFT . . . . . Density Functional Theory
DFTB . . . . . Density Functional Tight Binding
VASP . . . . . Vienna ab initio Simulation Package
XRD . . . . . X-RAY Diffraction
HOMO . . . . . Highest Occupied Molecular Orbital
LUMO . . . . . Lowest Unoccupied Molecular Orbital
OA . . . . . Oleic Acid
OA^- . . . . . Oleate

CHAPTER 1

INTRODUCTION

Nanotechnology is one of the most quickly developing science fields today and an important field of research which aims to manipulate and understand the behavior of matter at atomic and molecular scales. The ideas behind nanoscience and nanotechnology were founded by physicist Richard Feynman at Caltech the lecture called "There's plenty of room at the bottom" [1]. He mentioned that it is theoretically possible to manipulate and control materials on a small scale. During the last few decades new trends in nanoscience and nanotechnology research have arisen worldwide. Today, nanotechnology has become a rapidly growing industry by producing a wide range of nanoscale materials and processes. If the size of a material is less than 100 nm, it is defined as a nanostructure and it exhibits a different variation of physical, chemical, electronic and optical properties than their bulk counterparts. Such structures are categorized as low-dimensional structures, e.g., quantum well, quantum wires and quantum dots. Over the past few decades, a great interest has been focused on the optical and electronic properties of semiconductor quantum dots (QDs) that have a size in the nanometer range. Their physical properties can be controlled by changing the size, morphology, core/shell formation and surface modification [2, 3]. Surface manipulation opens up new possibilities by exploiting the current developments in nanoscale technology. They are leading a completely new set of applications, particularly in the fields of electronics, optoelectronics and biology [4–7]. Bright emissions, solution processability, tunable color properties and also the stable nature of QDs offer the possibility for ideal applications of light emitting diodes (LEDs) [8]. In recent experimental studies, it was reported that it is possible to produce large quantities of colloidal quantum dots in the purpose of QD-LEDs in the way to commercialization and can be compared with commercial LEDs that are used in the current display and lighting technology [9]. The tunable optical properties make QDs a competent candidate to be used not only in photovoltaics and photoconduction devices, lighting and display technology, chemical gas sensors, telecommunications and computing [9–11] but also in DNA detection, cell sorting and tracking, in vivo imaging and diagnostics [12–14]. The importance of surface interactions with ligands attached to a monolayer of semiconductor QDs are represented in the next subchapter a brief summary of relevant studies.

1.1. Semiconductor Quantum Dots

Quantum dots (QD) are defined as semiconductor nanostructures that have a size in the range of 2-10 nm whose physical and chemical properties strictly depend on their size and structure [15]. The unique properties of QDs have gained substantial interest in the research and their properties can be explained by the quantum confinement effect. Semiconductor QDs are a new generation of luminescent nanocrystals possessing unique spectral properties. QDs can stimulate several different color emission spectra via a signal by tuning the particle size. Typical colloidal QDs have very broad continuos absorption throughout the visible region depending on the particle size [16].

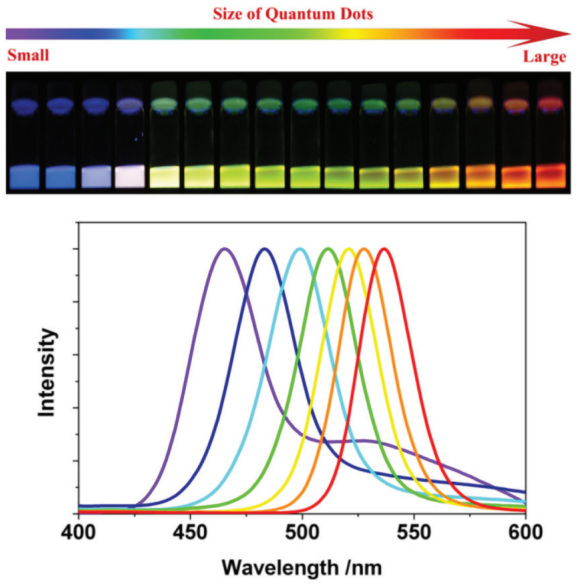

Figure 1.1. Tuning CdSe QD optical parameters by modifying the particle size. The different emission colors are observed between small and large CdSe QDs stimulated by a lamp with the nanoparticle size ranging from 1 to 10 nm. Smaller QDs have blue color while larger ones has a red color in near ultraviolet range. Adapted from [17].

Figure 1.1 demostrates the tunability of QDs by modifying their size. [17]. CdSe QDs exhibit different color emissions with different particle sizes. The photoluminescence (PL) emission wavelengths change depending on the size of CdSe QDs in the visible range of electromagnetic spectrum. The inner part of a QD is the core which can be composed of group II and VI elements such as CdTe, CdSe, ZnSe, ZnS and CdS or group III and V elements such as InAs and InP [18]. The II-VI semiconductors may exhibit

promising luminescent properties due to their direct band gap. Typical size of collodial QDs is a few nanometers, and they exhibit distinct narrow optical line spectra. One of the fundamental properties of QDs is that the energy band gap increases and that the blue shift increases when upon decreasing the particle size due to quantum confinement effect [19]. The effect allows one to fine-tune the band gap by changing the composition of semiconductor QDs. Additionally, the composition of the semiconductor material is as an essential aspect as its size when it comes to fine-tuning the bandgap and hence the density of states (DOS). Figure 1.2 illustrates a schematic representation of different dimensionalities and comparison of density of states (DOS) of three dimensional (3D), two dimensional (2D), one dimensinal (1D) and zero dimensional (0D) electron systems.

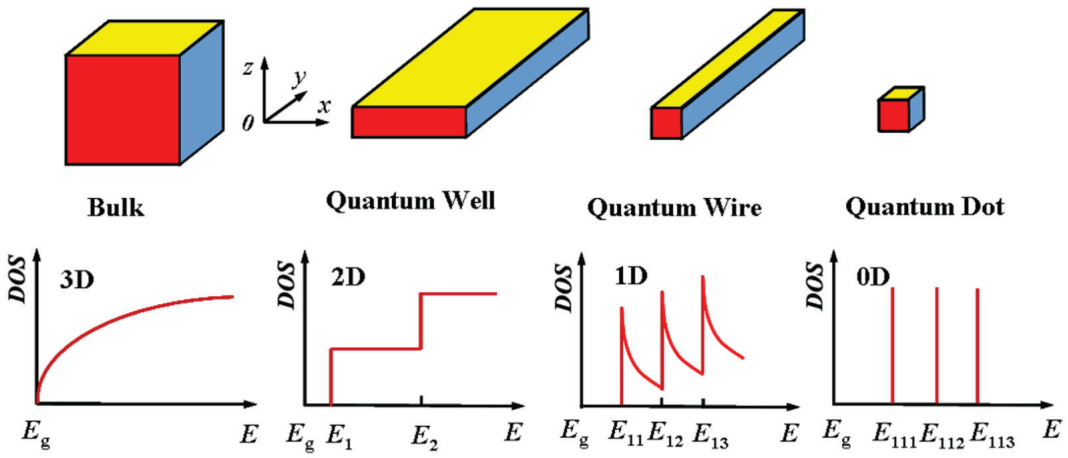

Figure 1.2. Schematic representation of low dimensional structures along with their corresponding density of states (DOS). Adapted from [20].

The density of states affects significantly optical properties such as absorption and emission. The density of states for free electrons in 3D structures, namely bulk structures are continuous energy levels and they do not exhibit quantum confinement effect. Quantum dots (0D) compared to the other low dimensional structures, they have quantized or discrete energy levels in density of states, this is case associated with their size [21]. These quantized energies and the confined material's dot-like form is what gives its name to the quantum dot. The quantized energy states make QDs a very unique structure for research. The effect of confinement generally results in an increase in the band gap with decreasing QD size. The exact effect on the resulting energy states of a material can be obtained with the solutions of the *Schrödinger* equation for the carriers in a confined space. This method is the most commonly used model for predicting quantum confinement, based on

the *Particle in a Box Model*. Assume that a particle is completely free between two infinite potential barriers in a box. In the box, the particle has no potential energy, the only energies are given by

$$E_n = \frac{n^2\pi^2\hbar^2}{2mL^2} \quad n = 1, 2, 3... \tag{1.1}$$

where the reduced mass is m and L is the length of the box. Each permitted energy is called an energy level and n is called the quantum number that represents an energy level E_n. The energy levels of these discrete states are inversely proportional to the square of L. For quantum dots, m is the effective mass of the electron and the hole and L is the particle diameter.

1.2. Surfaces of Semiconductor Quantum Dots

Another significant feature of QDs is that their properties are greatly influenced by the increased surface to volume ratio. Due to increased surface area of QDs, surface states are formed in which quantum states are associated with the surface. When the surface to volume ratio is high, the optical and electronic properties of QDs can be tuned by these surface states. In a recent study, it was reported that surface atoms constitute 15% of a CdSe QD with a diameter of 5 nm. [22]. Nanoparticles with such a high surface to volume ratio have a high surface site density, which may allow higher or lower transfer rates of photogenerated charging carriers. In semiconductor QDs, surface states can affect several properties such as the absorption, lifetime, spectrum and efficiency [23]. On the surface, the dangling bonds can generally be emerged by surface states of QDs, and nonstoichiometry and vacancies can affect them. At the QDs, these energies, which often extend into band voids, are due to these surface states [24].

Surface states have a major impact on various properties of QDs. Therefore, passivation of surface dangling bonds clears the gap to confine QD charge carriers and can enhance optical properties of QDs. Surface defects in QDs function for the electron, hole or excitons as temporary " traps " [21]. As a result, the radiative recombination can be quenched and the quantum yields (QYs) can be reduced by them. In order to develop photostable QDs, surface passivation is a very important issue. However, the surface manipulation of QDs is very compelling and is usually applied by introducing organically or inorganically capped QDs [25]. Ligands which are organic and inorganic molecules play a highly effective role on semiconductor nanoparticles in QD synthesis by tuning the size, composition and morphology of nanocrystals [26–29]. They are also crucial for

surface passivation by eliminating electronic traps [30]. Organic ligands bound to the nanocrystal surface and act as capping agents [31, 32]. The ligands can also be used by electronically coupling to the frontier orbitals at the interface of QD-ligand to control the electronic structure of the QD. Additionally, the dynamics excitation decay are affected by mediating charge trapping via ligands [33]. The most widely used organic ligands in QD synthesis are phosphonic acids, carboxylic acids, oleic acid and alkylthiols. The main purpose of ligands is to provide stability to the resulting QDs by preventing their agglomeration and also to make them soluble in organic solvents [34]. In many theoretical and experimental studies, oleic acid is a commonly used ligand for semiconductor quantum dots and nanocrystals (NCs); CdSe QDs, ZnS NCs, CdSe/ZnS core-shell structured nanocrystals and ternary alloy ZnCdS nanoparticles are some of the examples [35–40]. In experimental studies, the interaction between the ligand and semiconductor nanocrystal surfaces may seem to be generally understandable. However, ligand treatment and surface modification techniques cannot be adequately explained as seen in a model and remain a mystery. For realistic systems, it is necessary to understand the structural chemistry of interactions between ligands and quantum dots.

In this thesis, we investigate excitation dynamics on ZnS surface which are capped by oleic acid (OA) molecule for Zn and S rich surfaces. First, we use a simplified model to investigate the fundamental properties in the time dependent occupancy of a reservoir with frontier molecular orbitals. According to the results of the simplified model, it helped us understand how to proceed in the realistic system. Secondly, ZnS (111) surface is passivated by OA molecule and its different configurations are calculated using the density functional theory based tight binding method with Green's functions. The effect of different configurations of OA molecule are obtained on the spectra of highest occupied and lowest unoccupied molecular orbitals (HOMO and LUMO). The time dependent occupancy of the HOMO and the LUMO levels are calculated using the spectra results.

The thesis is organized as follows: The computational methods will be explained in Chapter 2. X-Ray diffraction patterns (XRD) of the quaternary $Zn_{1-x}Cd_xS_{1-y}Se_y$ nanoalloys will be given in Chapter 3. The simulation model, methodology and results for the simplified model and realistic systems will be presented and analyzed in Chapter 4. Our findings will be summarized in Chapter 5.

CHAPTER 2

COMPUTATIONAL METHODS

In this chapter, two methods that density functional theory and density functional tight binding method, and surface Green's function approach will be presented briefly in the following sections.

2.1. Density Functional Theory

Density functional theory (DFT) is a quantum mechanical method which is widely used method in computational physics, chemistry and materials science in order to study electronic structure of many-body systems, particularly atoms, molecules and the condensed phases. The idea behind this method is to write all terms making up the total energy in terms of ground state electron density. In this theory, properties of a many-electron system's properties can be designated by using functionals (functions of another function) that is based on the electron density. In practice, DFT is applied to investigate the structural, magnetic and electronic properties of condensed matter systems. Since DFT includes no empirical parameters that are derived from experimental data, it is said to be a first-principles method.

2.1.1. The Many-body Hamiltonian

In quantum mechanics, all knowledge can be attained from wavefunctions. In return, the Schrödinger equation is solved to acquire the wavefunctions. The fundamental requirement to determine the eigenfunctions of the many-body Hamiltonian

$$\hat{H}\psi(\vec{r_1},\ldots,\vec{r_N};\vec{R_1},\ldots,\vec{R_M}) = E\psi(\vec{r_1},\ldots,\vec{r_N};\vec{R_1},\ldots,\vec{R_M}) \tag{2.1}$$

where ψ, E and $\hat{H}$ represent the wavefunction, energy eigenvalue and Hamiltonian of the system, respectively. Morever, $\vec{r_i}$ is the position of electrons and $\vec{R_I}$ is the position of

nuclei. The many-body Hamiltonian can be written as follows,

$$\hat{H} = \hat{T} + \hat{V} \tag{2.2}$$

where $\hat{T}$ is the kinetic term and $\hat{V}$ is the potential term. The kinetic term has the kinetic energy of nuclei $\hat{T}_n$ and the kinetic energy of electrons $\hat{T}_e$. The potential term has nucleus-nucleus interaction $\hat{V}_{nn}$, electron-electron interaction $\hat{V}_{ee}$ and nucleus-electron interaction $\hat{V}_{ne}$. These terms form the Hamiltonian,

$$\hat{H} = \hat{T}_n + \hat{T}_e + \hat{V}_{nn} + \hat{V}_{ee} + \hat{V}_{ne}. \tag{2.3}$$

Explicity,

$$\hat{H} = -\frac{\hbar^2}{2m_n}\sum_{I=1}^{N_n}\nabla_I^2 - \frac{\hbar^2}{2m_e}\sum_{i=1}^{N_e}\nabla_i^2 + \frac{1}{2}\frac{e^2}{4\pi\epsilon_0}\sum_{I=1}^{N_n}\sum_{J\neq I}^{N_n}\frac{Z_I Z_J}{\left|\vec{R_I} - \vec{R_J}\right|} + \frac{1}{2}\frac{e^2}{4\pi\epsilon_0}\sum_{i=1}^{N_e}\sum_{j\neq i}^{N_e}\frac{1}{|\vec{r_i} - \vec{r_j}|} - \frac{e^2}{4\pi\epsilon_0}\sum_{i=1}^{N_e}\sum_{I=1}^{N_n}\frac{Z_I}{|\vec{r_i} - \vec{r_I}|} \tag{2.4}$$

where j and i represent to positions of electrons and J and I represent positions of nuclei. N_e and N_n represents the number of nuclei and electrons, respectively. Also, Z_I and Z_J are nuclei that are located at positions $\vec{R_I}$ and $\vec{R_J}$. The factor $1/2$ is necessary to avoid double counting the nucleus-nucleus and electron-electron interaction.

The Equation 2.4 is written in SI units. Therefore, each term includes inconvenient combinations of the fundamental constants; $\hbar$ (Planck constant), m (mass of an electron), e (charge of an electron) and ϵ_0 (the permittivity of free space). Hence, atomic units (a.u) are employed to simplify the expression. In a.u, $\hbar = m_e = 1/4\pi\epsilon_0 = 1$ and the fundamental the energy and the length are measured in terms of Hartree and the Bohr radius, respectively.

The exact, stationary and non-relativistic many-body Hamiltonian can be written in a.u in Equation 2.5,

$$\hat{H} = -\frac{1}{2}\sum_{I=1}^{N_n}\frac{1}{m_n}\nabla_I^2 - \frac{1}{2}\sum_{i=1}^{N_e}\nabla_i^2 + \frac{1}{2}\sum_{I=1}^{N_n}\sum_{J\neq I}^{N_n}\frac{Z_I Z_J}{\left|\vec{R_I} - \vec{R_J}\right|} + \frac{1}{2}\sum_{i=1}^{N_e}\sum_{j\neq i}^{N_e}\frac{1}{|\vec{r_i} - \vec{r_j}|} - \sum_{i=1}^{N_e}\sum_{I=1}^{N_n}\frac{Z_I}{|\vec{r_i} - \vec{r_I}|}. \quad (2.5)$$

In Equation 2.5, the many-body Hamiltonian includes the terms of electrons and nuclei in quantum mechanics. Essentially, the mass of the nucleus is considerably heavier than the mass of the electron. Therefore, one approach is used to solve this problem. This approach is called the Born-Oppenheimer approximation [41]. A nucleus cannot move quickly like an electron. Therefore, the nuclei act as $fixed$ particles in DFT calculations. As a result, two important derivations are achieved. One of them is that the kinetic energy of the nuclei is neglected.

Another point is that the potential term of nucleus-nucleus interaction is a constant. Depending on this approximation, the wavefunction includes the electronic part and the nuclei part as:

$$\psi(\vec{r}, \vec{R}) = \sum_i \phi_n(\vec{R})\psi_{el}(\vec{r}, \vec{R}) \quad (2.6)$$

where the term $\phi_n(\vec{R})$ is the nuclei wavefunction and $\psi_{el}(\vec{r}, \vec{R})$ is the electronic wavefunction. We concentrate on the electronic Hamiltonian, which includes the kinetic energy of electrons, electron-electron and nucleus-electron interaction terms, which is given as

$$\begin{aligned}\hat{H} &= \hat{T}_e + \hat{V}_{ee} + \hat{V}_{ne} \\ &= -\frac{1}{2}\sum_{i=1}^{N_e}\nabla_i^2 + \frac{1}{2}\sum_{i=1}^{N_e}\sum_{j\neq i}^{N_e}\frac{1}{|\vec{r_i} - \vec{r_j}|} - \sum_{i=1}^{N_e}\sum_{I=1}^{N_n}\frac{Z_I}{|\vec{r_i} - \vec{r_I}|}.\end{aligned} \quad (2.7)$$

Other approximations follow the Born-Oppenheimer approximation. These are Hartree and Hartree-Fock approximations. The idea of the Hartree approximation is that electrons are acknowledged to occupy different orbitals, because two electrons cannot exist in the same quantum state [42]. In the Hartree approximation, the electronic wave-

function can be shown as a part of single particle wavefunctions

$$\psi(x_1, x_2, \ldots, x_N) = \phi_1(x_1)\phi_2(x_2)\ldots\phi_N(x_N) \tag{2.8}$$

where the system has N electrons. Calculating the variational lowest energy from Equation 2.8 is a simple task. This approach, however, has a crucial shortcoming. It is unable to satisfy the antisymmetry requirement. This mean that when two arguments are exchanged the total wavefunction label occurs as:

$$\begin{aligned} P_{ij}\psi(x_1, \ldots, x_i, \ldots, x_j, \ldots, x_N) &= \psi(x_1, \ldots, x_j, \ldots, x_i, \ldots, x_N) \\ &= -\psi(x_1, \ldots, x_i, \ldots, x_j, \ldots, x_N). \end{aligned} \tag{2.9}$$

In Equation 2.9, the particle positions change with the exchange operator P. This is a demonstration of the Pauli exclusion principle. When this operator is applied one times on the wavefunction for fermions, the sign of the total wavefunction changes. Hence, the property of the Hartree approximation is not suitable. In order to satisfty the antisymmetry condition, Hartree and Fock suggest a notive approximation [43]. Generating the total wavefunction considering the interactions of electron exhange was proposed by Fock.

$$\psi_{HF} = \frac{1}{\sqrt{N!}}[\phi_1(x_1)\phi_2(x_2)\ldots\phi_N(x_N) - \phi_1(x_2)\phi_2(x_1)\ldots\phi_N(x_N) + \ldots] \tag{2.10}$$

Soon after that Slater determinant yields [44],

$$\psi_{HF}(x_1, ..., x_N) = \frac{1}{\sqrt{N!}} \begin{vmatrix} \phi_1(x_1) & \phi_1(x_2) & \ldots & \phi_1(x_N) \\ \phi_2(x_1) & \phi_2(x_2) & \ldots & \phi_2(x_N) \\ \vdots & \vdots & \ddots & \vdots \\ \phi_N(x_1) & \phi_N(x_2) & \ldots & \phi_N(x_N) \end{vmatrix} \tag{2.11}$$

where the factor $1/\sqrt{N!}$ is the normalization coefficient and N is the number of electrons. As a summary, the Hamiltonian is modified using the Hartree-Fock method. Quantum mechanically, the requirement of the indistinguishability and the electron exchange properties are satisfied.

2.1.2. The Electron Density

In quantum mechanics, the compelling task is to solve directly the Schrödinger equation and it only explains for hydrogen atom because of consisting of a nucleus and just one electron. However, an alternative solution can be offered by DFT. The total energy can be written in terms of the ground state electron density. This stage supplies a simplification due to decreasing the number of degrees of freedom. This energy can be determined a unique functional of electron density. In the system, the electronic density operator can be written as a measure of the contribution from each electron defined by

$$\hat{\rho}(\vec{r}) = \sum_{i}^{N} \delta(\vec{r} - \vec{r_i}) \tag{2.12}$$

where i is the electron index ($i = 1, 2, 3, \ldots, N$). So that, it provides to find the probably an electron in three dimensional space at $\vec{r_i}$ positions of the i^{th} electron. Substituting Equation 2.12 into the many-body wavefunction gives the electron density of the system

$$\begin{aligned} \rho(\vec{r}) =& \langle \psi(\vec{r_1}, \ldots, \vec{r_N}) | \hat{\rho}(\vec{r}) | \psi(\vec{r_1}, \ldots, \vec{r_N}) \rangle \\ =& \sum_{i}^{N} \int \delta(\vec{r} - \vec{r_i}) |\psi(\vec{r_1}, \vec{r_2}, \ldots, \vec{r_n})|^2 d\vec{r_1} d\vec{r_2} \ldots d\vec{r_N}. \end{aligned} \tag{2.13}$$

Applying the δ-function integrals over each variable and the expectation value of the density operator gives the electron density,

$$\rho(\vec{r}) = N \int |\psi(\vec{r}, \ldots, \vec{r_N})|^2 d\vec{r_2} \ldots d\vec{r_N}. \tag{2.14}$$

Assume that the wavefunction is normalized, the integral of $\rho(\vec{r})$ over all space yields the total number of electrons (N),

$$\int \rho(\vec{r}) d\vec{r} = N. \tag{2.15}$$

2.1.3. Energy in Terms of Density

In the system, all terms can be written in terms of density corresponding to the ground state. Hamiltonian can be described using the density operator and the expectation value of H_e is given as,

$$\begin{aligned} H_e &= \langle \psi(\vec{r_1}, \ldots, \vec{r_N}) | \, \hat{H}_e \, | \psi(\vec{r_1}, \ldots, \vec{r_N}) \rangle \\ &= \langle \psi(\vec{r_1}, \ldots, \vec{r_N}) | \, \hat{T}_e \; + \; \hat{V}_{ee} \; + \; \hat{V}_{ne} \, | \psi(\vec{r_1}, \ldots, \vec{r_N}) \rangle \, . \end{aligned} \tag{2.16}$$

Beginning with the kinetic energy term:

$$\begin{aligned} T_e &= \langle \psi(\vec{r_1}, \ldots, \vec{r_N}) | \, \hat{T}_e \, | \psi(\vec{r_1}, \ldots, \vec{r_N}) \rangle \\ &= -\frac{1}{2} \sum_{i=1}^{N_e} \int \psi^*(\vec{r_1}, \ldots, \vec{r_N}) \, \bigtriangledown_i^2 \, \psi(\vec{r_1}, \ldots, \vec{r_N}). \end{aligned} \tag{2.17}$$

This expectation value of the kinetic energy term is the most difficult to deal with because it includes a derivative operator. A methodology based on single-particle operator must be made to make contact with electronic density. Kohn and Sham proposed the approach that an auxiliary system of non-interacting particles can be found for each N-particle system in such a way that it has the same density with the ground state [45]. The electronic density is expressed as the sum of single-particle orbitals, namely *Kohn-Sham* orbitals (ϕ_i)

$$\rho(\vec{r}) = \sum_{i}^{N} |\phi_i(\vec{r})|^2 \tag{2.18}$$

By placing Equation 2.18 into Equation 2.17, kinetic energy in terms of single-particle orbitals is obtained, which is not equal to the kinetic energy of the real interacting system. Therefore, the kinetic energy can be defined as

$$T_e = -\frac{1}{2} \sum_{n}^{N_e} \int \phi_i^*(\vec{r}) \, \bigtriangledown^2 \, \phi_i(\vec{r}) d\vec{r} + \triangle T_e \tag{2.19}$$

where the first term is the single-particle kinetic energy and $\triangle T_e$ is a correction term to the non-interacting system for convenience between the auxiliary and the real system. The expectation value of the nucleus-electron energy term, V_{ne},

$$\begin{aligned} V_{ne} &= \langle \psi(\vec{r_1}, \ldots, \vec{r_N}) | \, \hat{V}_{ne} \, | \psi(\vec{r_1}, \ldots, \vec{r_N}) \rangle \\ &= -\sum_{i=1}^{N_e} \sum_{I=1}^{N_n} \int \frac{Z_I}{|\vec{r_i} - \vec{R_I}|} |\psi(\{\vec{r_1}, \ldots, \vec{r_N})|^2 d\vec{r_1}, \ldots, d\vec{r_N}. \end{aligned} \tag{2.20}$$

This term is rather easy since it does not contain any derivatives. Writing the summation over the electron index i and separating the terms, one obtains:

$$\begin{aligned} V_{ne} = -\sum_{I=1}^{N_n} \Bigg[\int \frac{Z_I}{|\vec{r_1} - \vec{R_I}|} d\vec{r_1} \int |\psi(\vec{r_1}, \ldots, \vec{r_N})|^2 d\vec{r_2} d\vec{r_3} \ldots d\vec{r_N} \\ + \int \frac{Z_I}{|\vec{r_2} - \vec{R_I}|} d\vec{r_2} \int |\psi((\vec{r_1}, \ldots, \vec{r_N})|^2 d\vec{r_1} d\vec{r_3} \ldots d\vec{r_N} + \ldots \Bigg]. \end{aligned} \tag{2.21}$$

As a result of manipulating this integral, the expectation value of the nucleus-electron interaction, V_{ne} becomes:

$$V_{ne} = -\sum_{I=1}^{N_n} \int \rho(\vec{r}) \frac{Z_I}{|\vec{r} - \vec{R_I}|} d\vec{r} = \int \rho(\vec{r}) \hat{V}_{ne} d\vec{r}. \tag{2.22}$$

The final term is the expectation value of the electron-electron interaction, V_{ee},

$$V_{ee} = \frac{1}{2} \int \int \frac{\rho(\vec{r}) \rho(\vec{r'})}{|\vec{r} - \vec{r'}|} d\vec{r} d\vec{r'} + \triangle V_{ee}. \tag{2.23}$$

In the end, all expectation values are found in terms of density. The total energy in the ground state of a system becomes,

$$E_{el} = T_e + V_{ne} + V_{ee}, \tag{2.24}$$

Explicity,

$$E_{el} = T_e + V_{ne} + V_{ee} = -\frac{1}{2}\sum_{n}^{N_e}\int \phi_i^*(\vec{r}) \bigtriangledown^2 \phi_i(\vec{r})d\vec{r} + \int \rho(\vec{r})\hat{V}_{ne}d\vec{r} + \frac{1}{2}\int\int \frac{\rho(\vec{r})\rho(\vec{r'})}{|\vec{r}-\vec{r'}|}d\vec{r}d\vec{r'} + \underbrace{\triangle T_e + \triangle V_{ee}}_{E_{xc}} \quad (2.25)$$

where the last two terms of correction are known as the exchange-correlation energy, E_{xc} is emerged from the difference between the potential and kinetic energy of the non-interacting and interacting system.

2.1.4. The Hohenberg-Kohn Theorems and Kohn-Sham Equations

Hohenberg and Kohn proposed and proved two basic theorems in 1964 [46]. Their first theorem designates that there is one-to-one correspondence between electronic ground-state density and external potential, $V_{ext}(\vec{r})$. To prove this theorem, it is necessary to consider two different potentials leading to the same ground state density, $n_0(\vec{r})$. These two potentials V_1^{ext} and V_2^{ext} with different ground state wavefunctions ψ_1 and ψ_2 lead to two different Hamiltonians $\hat{H}_1$ and $\hat{H}_2$, respectively. Since ψ_2 is not the ground state of $\hat{H}_1$, one obtains such as:

$$E_1 = \langle\psi_1|\,\hat{H}_1\,|\psi_1\rangle < \langle\psi_2|\,\hat{H}_1\,|\psi_2\rangle\,. \quad (2.26)$$

Here, unless the ground state is degenerate, the inequality arises by following the arguments of Hohenberg and Kohn. Assume that both potentials create the same ground state, the last term in Equation 2.26 can be written as:

$$\underbrace{\langle\psi_2|\,\hat{H}_1\,|\psi_2\rangle}_{>E_1} = \underbrace{\langle\psi_2|\,\hat{H}_2\,|\psi_2\rangle}_{E_2} + \int d\vec{r}\Big[V_1^{ext}(\vec{r}) - V_2^{ext}(\vec{r})\Big]n_0(\vec{r}). \quad (2.27)$$

Similarly,

$$\underbrace{\langle\psi_1|\,\hat{H}_2\,|\psi_1\rangle}_{>E_2} = \underbrace{\langle\psi_1|\,\hat{H}_1\,|\psi_1\rangle}_{E_1} + \int d\vec{r}\Big[V_2^{ext}(\vec{r}) - V_1^{ext}(\vec{r})\Big]n_0(\vec{r}). \tag{2.28}$$

Consequently, the summing up of Equation 2.27 and Equation 2.28 clearly contradicts the fact that two different external potentials can not lead to the same ground density.

$$E_1 + E_2 < E_2 + E_1. \tag{2.29}$$

Their second theorem is that a *"universal functional"* for the energy $E[\rho]$ can be defined in terms of density, valid for any $V_{ext}(\vec{r})$. The global minimum of this functional can be found by invoking the variational principle as described in the Hartree-Fock approach. This time, it applied the density that minimizes the energy functional, and it yields the exact ground state density.

Additionally, the density other than the density of the ground state can not provide less energy than the ground state energy:

$$E[\rho] > E_0[\rho_0] = E_0 \tag{2.30}$$

where E_0 represents the energy of the ground state, ρ_0 and ρ represent the density of the ground state and some random state, respectively.Equation 2.30 then leads to

$$\langle\psi|\,\hat{H}\,|\psi\rangle = T_e[\rho] + V_{ee}[\rho] + \int \rho(\vec{r})V_{ext}d\vec{r} = E[\rho] \geqslant E_0[\rho] = \langle\psi_0|\,\hat{H}\,|\psi_0\rangle\,. \tag{2.31}$$

The theorems of Hohenberg-Kohn guarantee that total energy is a functional of the electron density in the ground state of the system. Reorganizing Equation 2.25 and the total energy in terms of density can finally be written in Equation 2.32,

$$
\begin{aligned}
E_{el}[\rho(\vec{r})] &= T_e[\rho(\vec{r})] + V_{ne}[\rho(\vec{r})] + V_{ee}[\rho(\vec{r})] \\
&= -\frac{1}{2}\sum_{n}^{N_e}\int \phi_i^*(\vec{r}) \bigtriangledown^2 \phi_i(\vec{r}) d\vec{r} + \int \rho(\vec{r})\hat{V}_{ne} d\vec{r} \\
&+\frac{1}{2}\int\int \frac{\rho(\vec{r})\rho(\vec{r'})}{|\vec{r}-\vec{r'}|} d\vec{r} d\vec{r'} + E_{xc}[\rho(\vec{r})]
\end{aligned} \tag{2.32}
$$

where E_{xc} refers the exchange and correlation term for electron. The consequence of the theorems that reduce this energy gives wavefunction of the ground state. Minimizing the energy is achieved by adding one derivative to Equation 2.32 corresponding with non-interacting, called *Kohn-Sham* (KS) orbitals. Functional derivative yields:

$$
\frac{\delta E}{\delta \phi_i^*(\vec{r})} = \frac{\delta T_e}{\delta \phi_i^*(\vec{r})} + \left[\frac{\delta E_{ext}}{\delta n(\vec{r})} + \frac{\delta E_{Hartree}}{\delta n(\vec{r})} + \frac{\delta E_{xc}}{\delta n(\vec{r})}\right]\frac{\delta n(\vec{r})}{\delta \phi_i^*(\vec{r})} = \epsilon_i \phi_i(\vec{r}). \tag{2.33}
$$

Kohn-Sham energies are defined as eigenvalues ϵ_i terms that hold ϕ_i orthogonal during minimization. Equation 2.33 gives as,

$$
-\frac{1}{2} \bigtriangledown^2 \phi_i^2(\vec{r}) + \left[V_{ext}(\vec{r}) + \int d\vec{r'} \frac{n(\vec{r'})}{|\vec{r}-\vec{r'}|} + V_{xc}\right]\phi_i(\vec{r}) = \epsilon_i \phi_i(\vec{r}), \tag{2.34}
$$

briefly,

$$
\left[\hat{T} + V_{eff}\right]\phi_i(\vec{r}) = \epsilon_i \phi_i(\vec{r}) \tag{2.35}
$$

where V_{eff} involves $V_{Hartree}$, V_{xc} and V_{ext} on the reference orbital $\phi_i(\vec{r})$ in a mean-field-like manner. The Hartree potential, $V_{Hartree}$, is electron-electron interaction, V_{ext} is the external potential due to the nuclei and any other external fields and V_{xc} defines the exchange-correlation potential. Since all the potential terms depend on the density, the KS equations need to be solved iteratively using a self-consistent procedure as in Figure 2.1. This iteration continues until a predetermined convergence value is reached by the calculation. If the initial estimate $n_0(\vec{r})$ is a good value, convergence can be significantly accelerated.

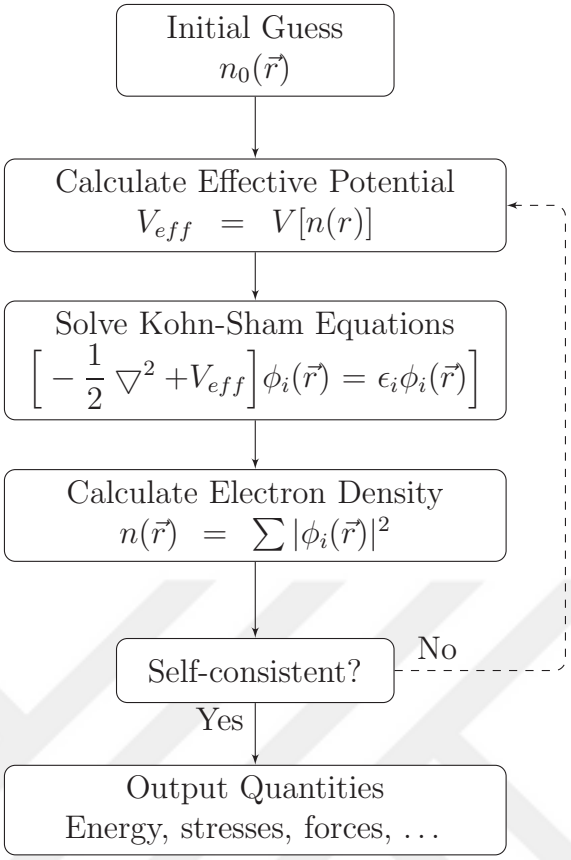

Figure 2.1. The presentation of self-consistency calculations in the flow chart. The schematic diagram is inspired from [47].

2.1.5. Exchange and Correlations Functionals

Kohn-Sham orbitals describe every term of energy in the many body Hamiltonian. The exchange-correlations in term of the density is not exactly known, so that this term is still a diffucult task. In order to make the calculation more accurate, it should be approached in such as the effects of exchange and correlation, which are captured correctly. There are many possible approaches. One of them is the Local Density Approach (LDA) [48]. It is the easiest and most widely used method. In addition this approach, there are several improved methods for approaching the energy of exchange and correlation to make the calculation more accurate, such as Generalized Gradient Approximation (GGA) [49].

2.2. Density Functional Tight Binding Method

Density functional tight binding (DFTB) is an approximate method, which is based on the density functional theory method used in many science areas. DFTB method is very popular because of its efficiency in large simulations. This method is used very widely in many applications such as calculations of constant of hyperfine coupling, solids and molecules vibrational spectra, tensors of nuclear magnetic shieldning, dynamic, magnetic and geometries properties. Also, the calculation of optical properties can be determined by using the time-dependent DFTB. DFTB is based on a second order expansion of the total energy of Kohn-Sham orbitals in DFT with regard to fluctuations in density. According to this approach, the reference electron density is acquired self-consistently from confined neutral atoms. Also, the confinement potential energy is obtained to estimate the effective potential and charge density for molecules and solids. DFTB is a tight binding method that does not need to have large amounts of empirical parameters. In addition, DFT calculation can be used to obtain the parameters.

The calculation of electronic structures was proposed by Slater and Koster for using the application of tight binding [50]. The concept behind this approach is to describe the atomic-like structure of Hamiltonian eigenstates. Also, the Hamiltonian is replaced by a parameterized Hamiltonian matrix that relies on the distances and orbital symmetries of its elements only. Initially developed to measure band structures in periodic systems, the Slater-Koster method was then generalized as an atomic model capable of treating finite systems. The DFTB method was developed to participate in three main requierements [51]:

(i) The Hamilton matrix elements must be functionally dependent on the interatomic distance in the first criterion. Froyen and Harrison have suggested to connect the interatomic distance by $1/r^2$ to the Hamiltonian matrix components [52]:

(ii) The goal of the second requirement that is not only for band energy but for the total energy. Chadi suggested that the total energy was separated into two parts,

$$E = E_{bnd} + E_{rep} \tag{2.36}$$

where E_{bnd} is the energies of all occupied orbitals, and E_{rep} represents the repulsive contribution [53].

E_{rep} is described by,

$$E_{rep} = \sum_{\alpha,\beta}^{N} U_{\alpha\beta} \tag{2.37}$$

where N is the number of atoms and the repulsive contribution is defined by the sum of the atomic pair terms.

(iii) The last prerequisite is to extract the atomic forces from the total energy, which is particularly important for optimizing geometry and molecular dynamics. The DFTB method has these requirements which avoids any empirical parametrization by calculating Hamiltonian and overlap matrices. Such matrices are determined using DFT derived atom-like valence orbitals. Using DFT as the basis for a tight binding method, electronic density is defined by

$$\rho(\vec{r}) = \rho_0(\vec{r}) + \delta\rho(\vec{r}). \tag{2.38}$$

Inserting this electron density into Equation 2.32:

$$\begin{aligned} E[\rho_0 + \delta\rho] = &\sum_{i}^{M} n_i \left\langle \psi_i \right| -\frac{1}{2}\bigtriangledown^2 + V_{ext}(\vec{r}) + \int \frac{\rho_0'}{|\vec{r} - \vec{r'}|} d\vec{r'} + V_{xc}[\rho_0] \left| \psi_i \right\rangle \\ &- \frac{1}{2}\int\int \frac{\rho_0'(\rho_0 + \delta\rho)}{|\vec{r} - \vec{r'}|} d\vec{r'}d\vec{r} - \int V_{xc}[\rho_0](\rho_0 + \delta\rho)d\vec{r} \\ &+ \frac{1}{2}\int\int \frac{\delta\rho'(\rho_0 + \delta\rho)}{|\vec{r} - \vec{r'}|} d\vec{r}d\vec{r'} + E_{xc}[\rho_0 + \delta\rho] + E_{nn} \end{aligned} \tag{2.39}$$

where ρ_0' equals to $\rho_0(\vec{r'})$ and $\delta\rho'$ equals to $\delta\rho(\vec{r'})$. In this equation, E_{nn} term describes the nuclear repulsion. The Taylor expansion of the exchange-correlation term, $E_{xc}[\rho_0 + \delta\rho]$, up to the second-order term:

$$E_{xc}[\rho_0 + \delta\rho] = E_{xc}[\rho_0] + \int \left.\frac{\delta E_{xc}}{\delta\rho}\right|_{\rho_0} \delta\rho d\vec{r} + \frac{1}{2}\int\int \left.\frac{\delta^2 E_{xc}}{\delta\rho\delta\rho'}\right|_{\rho_0} \delta\rho\delta\rho' d\vec{r}d\vec{r'}. \tag{2.40}$$

Substitution of Equation 2.40 into Equation 2.39 using the definition $(\delta E_{xc}/\delta\rho = V_{xc}[\rho])$ results as in Equation 2.41,

$$
\begin{aligned}
E = & \sum_{i}^{M} n_i \left\langle \psi_i \right| -\frac{1}{2}\bigtriangledown^2 + V_{ext}(\vec{r}) + \int \frac{\rho_0'}{|\vec{r}-\vec{r'}|} d\vec{r'} + V_{xc}[\rho_0] \left| \psi_i \right\rangle \\
& - \frac{1}{2}\int\int \frac{\rho_0'\rho_0}{|\vec{r}-\vec{r'}|} d\vec{r} d\vec{r'} + E_{xc}[\rho_0] - \int V_{xc}[\rho_0]\rho_0 d\vec{r} + E_{nn} \\
& + \frac{1}{2}\int\int \left(\frac{\delta\rho\delta\rho'}{|\vec{r}-\vec{r'}|} + \frac{\delta^2 E_{xc}}{\delta\rho\delta\rho'}\bigg|_{\rho_0} \right) d\vec{r} d\vec{r'}.
\end{aligned} \tag{2.41}
$$

In Equation 2.41, the terms in the first line describe the sum of the energies of all the orbitals occupied, E_{bnd}

$$
E_{bnd}[\rho_0] = \sum_{i}^{M} n_i \left\langle \psi_i \right| -\frac{1}{2}\bigtriangledown^2 + V_{ext}(\vec{r}) + \int \frac{\rho_0'}{|\vec{r}-\vec{r'}|} d\vec{r'} + V_{xc}[\rho_0] \left| \psi_i \right\rangle, \tag{2.42}
$$

and the terms in the second line of Equation 2.41 describe the repulsive contribution, E_{rep}

$$
E_{rep}[\rho_0] = -\frac{1}{2}\int\int \frac{\rho_0'\rho_0}{|\vec{r}-\vec{r'}|} d\vec{r} d\vec{r'} + E_{xc}[\rho_0] - \int V_{xc}[\rho_0]\rho_0 d\vec{r} + E_{nn}. \tag{2.43}
$$

In Equation 2.41, the last term involves corrections which depends on the fluctuations in the density. This term is called second-order correction term,

$$
E_{2nd}[\rho_0, \delta\rho] = \frac{1}{2}\int\int \left(\frac{\delta\rho\delta\rho'}{|\vec{r}-\vec{r'}|} + \frac{\delta^2 E_{xc}}{\delta\rho\delta\rho'}\bigg|_{\rho_0} \right) d\vec{r} d\vec{r'}. \tag{2.44}
$$

The second-order correction term, E_{2nd}, is neglected to solve without self consistency in the standard DFTB. The solution of the non-self-consistent DFTB is very suitable to investigate properties of polyatomic, for example, homonuclear systems. However, the second-order correction term can not be negligible when a more sensitive charge balance is tested for chemical bonds in the system such as heteronuclear molecules and polar semiconductors [54]. Then, the self-consistent charge correction DFTB is a more convenient way to better define electronic systems and boost DFTB transmission [55].

2.3. Surface Green's Function

The surface Green's function approach is provided to define the interface between different leads [56, 57]. We consider a system composed of a molecule M connected to one semi-infinite reservoir R as illustrated in Figure 2.2.

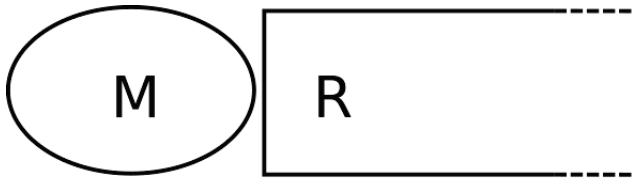

Figure 2.2. Schematic diagram of a molecule and semi-infinite reservoir.

The surface properties of the semi-infinite reservoir are obtained using Green's function approach. The molecule and the semi-infinite reservoir are described by the Hamiltonian H_{MM} and H_{RR}, respectively. The Hamiltonian H and overlap S matrices for the full system can be described in matrix form as follows:

$$H = \begin{pmatrix} H_{MM} & H_{MR} \\ H_{MR} & H_{RR} \end{pmatrix}, \quad S = \begin{pmatrix} S_{MM} & S_{MR} \\ S_{MR} & S_{RR} \end{pmatrix} \tag{2.45}$$

where the off-diagonal terms stand for the couplings between the molecule and the semi-infinite reservoir. The Green's function is expressed through the matrix multiplication $(\epsilon S - H)G = \mathbb{1}$ where $\epsilon = E + i\eta$ with η arbitrarily small, E is the energy variable and $\mathbb{1}$ is the identity matrix. The Green's function of the system can be partitioned into submatrices:

$$\begin{pmatrix} G_{MM} & G_{MR} \\ G_{RM} & G_{RR} \end{pmatrix} = \begin{pmatrix} \epsilon S_{MM} - H_{MM} & \epsilon S_{MR} - H_{MR} \\ \epsilon S_{RM} - H_{RM} & \epsilon S_{RR} - H_{RR} \end{pmatrix}^{-1}. \tag{2.46}$$

We get the numerically exact results for the Green's function of the semi-infinite reservoir using the iteravite calculation [56]. For one-dimensional semi-infinite reservoir,

the Hamiltonian and overlap matrices are in block tridiagonal form

$$H = \begin{pmatrix} H_{00} & H_{01} & 0 & \\ H_{01}^{\dagger} & H_{00} & H_{01} & \cdots \\ 0 & H_{01}^{\dagger} & H_{00} & \\ & \vdots & & \ddots \end{pmatrix}, \quad S = \begin{pmatrix} S_{00} & S_{01} & 0 & \\ S_{01}^{\dagger} & S_{00} & S_{01} & \cdots \\ 0 & S_{01}^{\dagger} & S_{00} & \\ & \vdots & & \ddots \end{pmatrix}. \tag{2.47}$$

The transfer matrices T and $\overline{T}$ can be easily calculated using the iterative procedure

$$T = t_0 + \tilde{t_0} t_1 + \tilde{t_0}\tilde{t_1} t_2 + \cdots + \tilde{t_0}\tilde{t_1}\tilde{t_2} \ldots t_n, \tag{2.48}$$

$$\overline{T} = \tilde{t_0} + t_0\tilde{t_1} + t_0 t_1 \tilde{t_2} + \cdots + t_0 t_1 t_2 \ldots \tilde{t_n}, \tag{2.49}$$

where t_i and $\tilde{t_i}$ are described with the recursion formulas:

$$t_i = (I - t_{i-1}\tilde{t}_{i-1} - \tilde{t}_{i-1} t_{i-1})^{-1} t_{i-1}^2, \tag{2.50}$$

$$\tilde{t_i} = (I - t_{i-1}\tilde{t}_{i-1} - \tilde{t}_{i-1} t_{i-1})^{-1} \tilde{t}_{i-1}^2. \tag{2.51}$$

Here,

$$t_0 = -(\epsilon S_{00} - H_{00})^{-1}(\epsilon S_{01}^{\dagger} - H_{01}^{\dagger}), \tag{2.52}$$

$$\tilde{t_0} = -(\epsilon S_{00} - H_{00})^{-1}(\epsilon S_{01} - H_{01}). \tag{2.53}$$

The process is repeated until t_n and $\tilde{t_n}$ are smaller than an arbitrarily small number for the accuracy of the calculation. Finally, the system Green's function can be written as

$$G(E) = \left[(\epsilon S_{00} - H_{00}) + (\epsilon S_{01}^{\dagger} - H_{01}^{\dagger})\overline{T} \right]^{-1}. \tag{2.54}$$

In particular, we can consider the expression the of the self-energies of the molecule and the reservoir as: $\Sigma = (\epsilon S_{01}^{\dagger} - H_{01}^{\dagger})\overline{T}$.

CHAPTER 3

QUATERNARY $Zn_{1-x}Cd_xS_{1-y}Se_y$ NANOALLOYS

The electronic and optoelectronic properties of QDs can be altered by alloying, even if the particle size stays the same. Even when the size of a QD is kept constant, the alloy materials allows to control the energy band gap. In this chapter, Density Functional Theory (DFT) calculations are performed in order to understand the trends of changes in the energy band gap with composition parameters x and y. Furthermore, the most suitable quaternary $Zn_{1-x}Cd_xS_{1-y}Se_y$ nanoalloys are selected according to the experimental results and the X-Ray diffraction (XRD) patterns of these quaternary nanoalloys are evaluated theoretically.

3.1. Bulk Materials

Due to the large number of atoms in QDs and the need to scan a wide parameter space in DFT calculations, the calculations are performed primarily in periodic systems. For this purpose, $2 \times 2 \times 2$ supercell from the primitive unit cell of the zinc blende (ZB) cubic structure are constructed. Figure 3.1 demostrates a unit cell of binary ZnS, CdS, ZnSe and CdSe bulk structures.

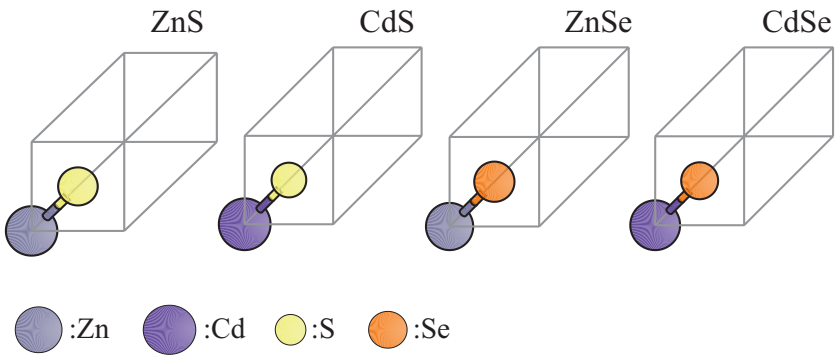

Figure 3.1. A unit cell of bulk ZnS, CdS, ZnSe and CdSe.

The electronic and structural properties of quaternary $Zn_{1-x}Cd_xS_{1-y}Se_y$ nanoalloys are optimized using by the Vienna Ab initio Simulation Package (VASP) by employing the projector augmented wave (PAW) method, in particular, the exchange and correlation functional of Perdew-Burke-Ernzerhof (PBE). Primarily, optimized lattice constants of binary ZnS, CdS, ZnSe and CdSe bulk structures are 2.723, 2.968, 2.867 and 3.101 Å, respectively (see Table 3.1 and Table 3.2).

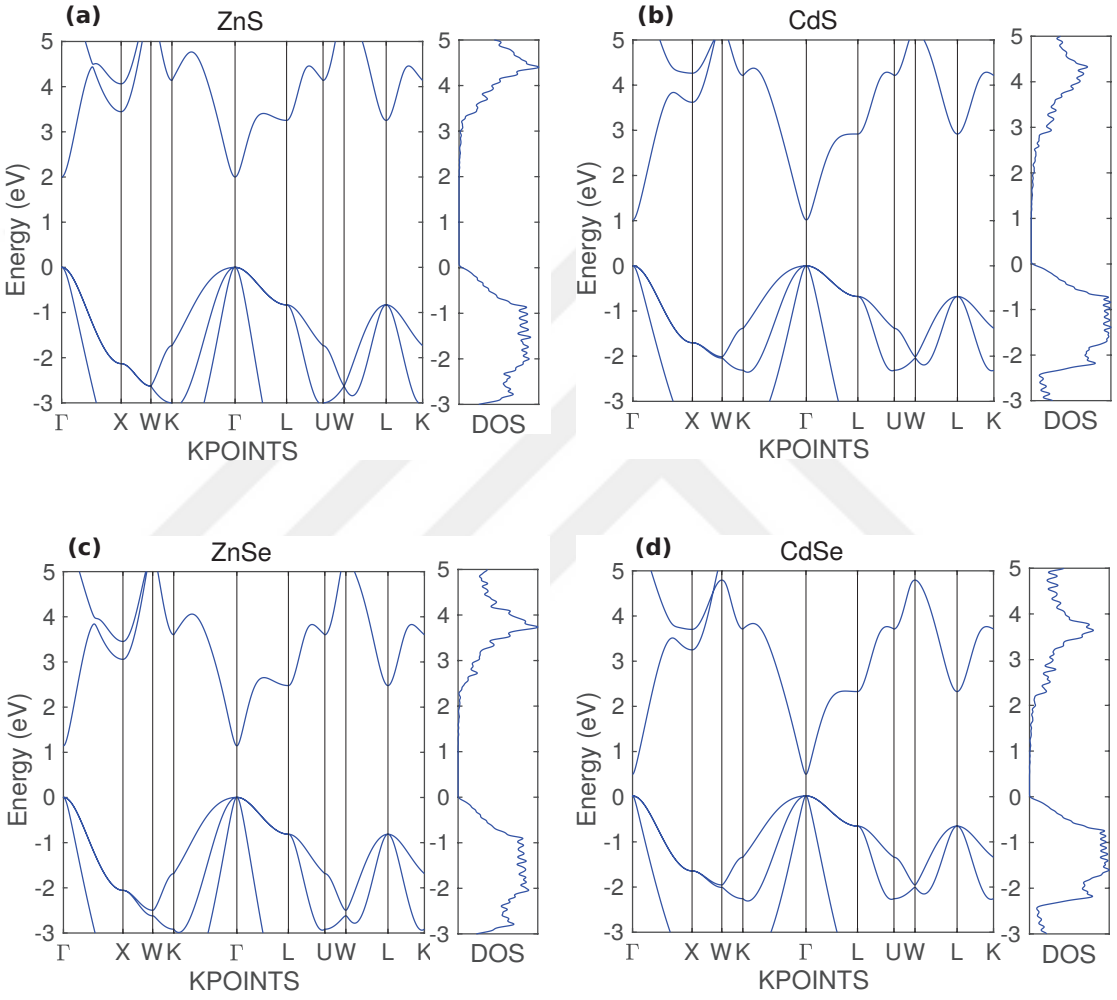

Figure 3.2. The band and DOS diagram for ZnS, CdS, ZnSe and CdSe.

The electronic band structures and density of states (DOS) of these bulk materials are represented as seen in Figure 3.2. The band gaps of binary ZnS, CdS, ZnSe and CdSe bulk structures are 2.061, 1.087, 1.236 and 0.599 eV, respectively. The total of 36 stoichiometries by assigning the value set of $\{0,0.125,0.25,0.50,0.75,1\}$ to x and y parameters are achieved. All possible atomic configurations in the alloy (677 configurations in total) are designed by considering system symmetries.

Table 3.1. The lattice constant (in Å), position(s), the minimum and maximum band gap (in eV) of $Zn_{1-x}Cd_xS_{1-y}Se_y$ quaternary alloys.

Material	Lattice constant	Position(s)	Band gap
ZnS	2.723	1	2.061
$Zn_{0.875}Cd_{0.125}S$	2.754	1	1.849
$Zn_{0.75}Cd_{0.25}S$	2.784	5	1.628-1.719
$Zn_{0.50}Cd_{0.50}S$	2.846	12	1.334-1.423
$Zn_{0.25}Cd_{0.75}S$	2.907	11	1.184-1.250
CdS	2.968	1	1.087
$ZnS_{0.875}Se_{0.125}$	2.741	1	1.884
$Zn_{0.875}Cd_{0.125}S_{0.875}Se_{0.125}$	2.772	6	1.593-1.722
$Zn_{0.75}Cd_{0.25}S_{0.875}Se_{0.125}$	2.802	32	1.365-1.609
$Zn_{0.50}Cd_{0.50}S_{0.875}Se_{0.125}$	2.863	45	1.126-1.314
$Zn_{0.25}Cd_{0.75}S_{0.875}Se_{0.125}$	2.924	37	1.014-1.159
$CdS_{0.875}Se_{0.125}$	2.985	1	0.984
$ZnS_{0.75}Se_{0.25}$	2.759	5	1.667-1.782
$Zn_{0.875}Cd_{0.125}S_{0.75}Se_{0.25}$	2.789	32	1.357-1.609
$Zn_{0.75}Cd_{0.25}S_{0.75}Se_{0.25}$	2.820	45	1.090-1.453
$Zn_{0.50}Cd_{0.50}S_{0.75}Se_{0.25}$	2.880	34	0.762-1.186
$Zn_{0.25}Cd_{0.75}S_{0.75}Se_{0.25}$	2.941	62	0.826-1.063
$CdS_{0.75}Se_{0.25}$	3.001	5	0.850-0.927
$ZnS_{0.50}Se_{0.50}$	2.795	12	1.411-1.486
$Zn_{0.875}Cd_{0.125}S_{0.50}Se_{0.50}$	2.825	45	1.157-1.339
$Zn_{0.75}Cd_{0.25}S_{0.50}Se_{0.50}$	2.855	34	0.935-1.205
$Zn_{0.50}Cd_{0.50}S_{0.50}Se_{0.50}$	2.915	22	0.674-1.078
$Zn_{0.25}Cd_{0.75}S_{0.50}Se_{0.50}$	2.975	30	0.659-0.847
$CdS_{0.50}Se_{0.50}$	3.035	5	0.693-0.744
$ZnS_{0.25}Se_{0.75}$	2.831	11	1.315-1.384
$Zn_{0.875}Cd_{0.125}S_{0.25}Se_{0.75}$	2.861	37	1.082-1.284
$Zn_{0.75}Cd_{0.25}S_{0.25}Se_{0.75}$	2.890	62	0.566-1.163
$Zn_{0.50}Cd_{0.50}S_{0.25}Se_{0.75}$	2.949	30	0.679-0.940
$Zn_{0.25}Cd_{0.75}S_{0.25}Se_{0.75}$	3.009	28	0.603-0.840
$CdS_{0.25}Se_{0.75}$	3.068	6	0.641-0.685

Table 3.2. The lattice constant (in Å), position(s), the minimum and maximum band gap (in eV) of $Zn_{1-x}Cd_xS_{1-y}Se_y$ quaternary alloys.

Material	Lattice constant	Position(s)	Band gap
ZnSe	2.867	1	1.236
$Zn_{0.875}Cd_{0.125}Se$	2.896	1	1.084
$Zn_{0.75}Cd_{0.25}Se$	2.926	5	0.917-1.004
$Zn_{0.50}Cd_{0.50}Se$	2.984	5	0.713-0.801
$Zn_{0.25}Cd_{0.75}Se$	3.043	6	0.636-0.703
CdSe	3.101	1	0.599

The lattice parameters of ternary and quaternary bulk are determined by linear interpolation based on optimized binary (ZnS, CdS, CdSe, ZnSe) compounds, depending on x and y values. Atomic positions in the structures are optimized so that the maximum force on the ions are less than 0.01 eV / Å and additionally, the convergence criterion on the total energy is chosen to be 10^{-5} eV. For all the calculations, the kinetic energy cutoff for plane wave basis set is taken to be 380 eV. The optimization of atomic positions is carried out in two stages. The Brillouin zone is sampled using the Monkhorst-Pack approach with $1 \times 1 \times 1$ followed by $6 \times 6 \times 6$ k-point grids. According to the test results, we performed calculations with a much denser k-grid such as $8 \times 8 \times 8$ and $10 \times 10 \times 10$ as long as our computational resources allow. The band gaps for binary, ternary and quaternary materials are obtained from the DOS as shown in Table 3.1 and Table 3.2. The stoichiometry, the number of configurations and the minimum and maximum values of the band gap ranges from these configurations are given in the respective columns of the mentioned tables. Figure 3.3 shows the band gap energy intervals of the bulk $Zn_{1-x}Cd_xS_{1-y}Se_y$ structures. The electronic band gap energy values of bulk $Zn_{1-x}Cd_xS_{1-y}Se_y$ materials are calculated for each of these materials by constructing possible positions. The average of the band gap energy values for the position of each nanoalloy is displayed in Figure 3.3(a). As a general trend, the band gap energy is obversed to decrease as high x and y parameters are reached. The minimum energy values of each nanoalloy in different positions are determined and the band gap energies of the materials with these minimum energy are investigated in Figure 3.3(b). We observe that the band gap increases when concentrations of Zn and S increase.

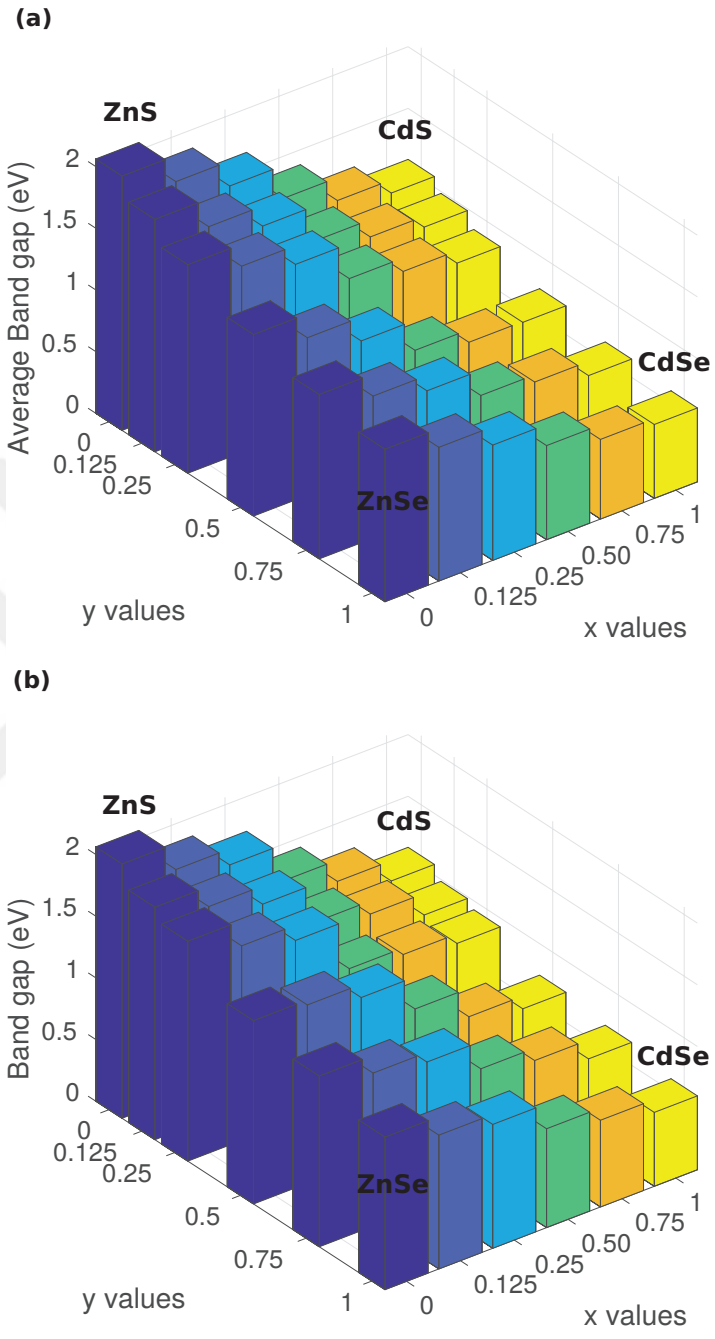

Figure 3.3. The band gap energies of bulk $Zn_{1-x}Cd_xS_{1-y}Se_y$ structures. (a) The average of band gaps in Table 3.1. (b) The band gaps of configurations having the minimum energy for each nanoalloy structures.

3.2. X-Ray Diffraction Spectra

X-Ray Diffraction (XRD) analysis was performed to understand the structural characterization of $Zn_{1-x}Cd_xS_{1-y}Se_y$ nanoalloys. XRD was simulated for optimized atomic configurations corresponding to the alloy composition parameters (x,y) used in the experiments. The XRD measurements are performed by using VESTA program. Alloy composition parameters for experimental studies, x is less than 0.50 and y is larger than 0.50. So, we chose suitable the quaternary ZnCdSSe nanoalloys in our study. Figue 3.4 shows XRD patterns of the $Zn_{0.50}Cd_{0.50}S_{0.75}Se_{0.25}$, $Zn_{0.50}Cd_{0.50}S_{0.50}Se_{0.50}$ and $Zn_{0.25}Cd_{0.75}S_{0.50}Se_{0.50}$ nanoalloy compositions.

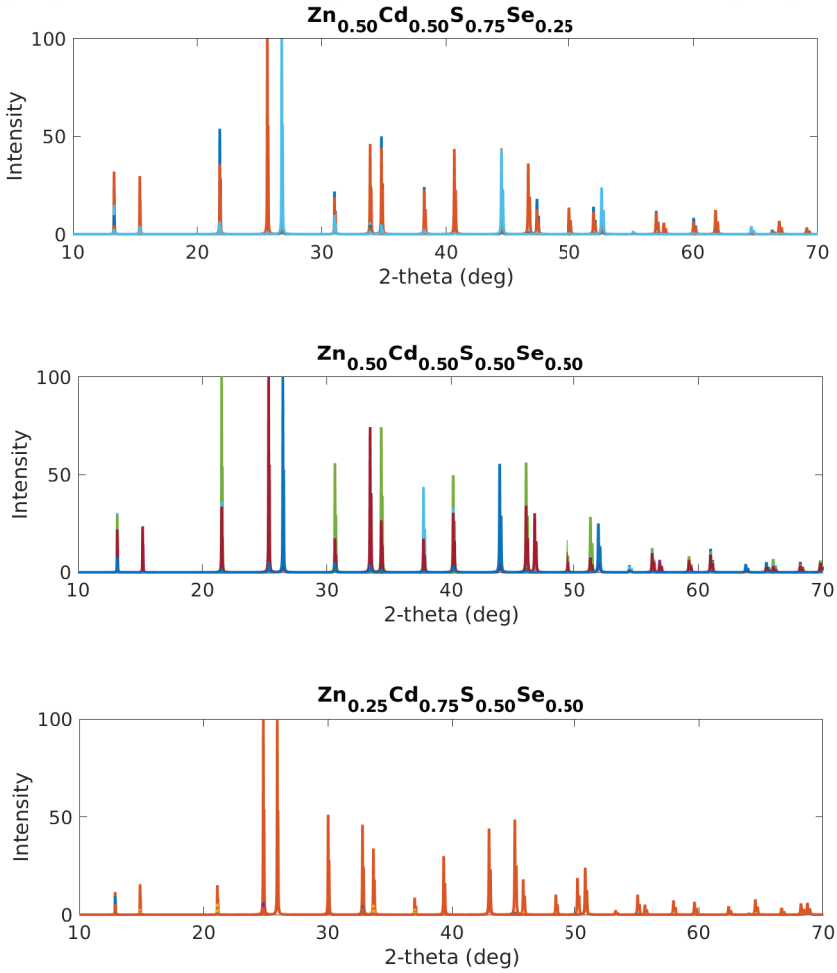

Figure 3.4. XRD patterns of $Zn_{0.50}Cd_{0.50}S_{0.75}Se_{0.25}$, $Zn_{0.50}Cd_{0.50}S_{0.50}Se_{0.50}$ and $Zn_{0.25}Cd_{0.75}S_{0.50}Se_{0.50}$ nanoalloy compositions consist of 34, 22 and 30 different positions, respectively.

$Zn_{0.50}Cd_{0.50}S_{0.75}Se_{0.25}$, $Zn_{0.50}Cd_{0.50}S_{0.50}Se_{0.50}$ and $Zn_{0.25}Cd_{0.75}S_{0.50}Se_{0.50}$ nanoalloy compositions have 34, 22 and 30 different configuration positions, respectively. According to XRD results, peaks of different positions for $Zn_{0.25}Cd_{0.75}S_{0.50}Se_{0.50}$ are not very different from each other. We mentioned that the simple equation is derived from the particle in a box model as given above in Equation 1.1. This equation is very useful in explaining the optical and electronic properties of nanoparticles. We performed that the material size and the effect of the alloy composition over mass can control the electronic properties of the colloidal alloy. We have constructed all structures of the same size supercell ($2 \times 2 \times 2$) by changing the composition alloy. We have observed that the material size can be kept constant, the band gaps of $Zn_{0.50}Cd_{0.50}S_{0.75}Se_{0.25}$, $Zn_{0.50}Cd_{0.50}S_{0.50}Se_{0.50}$ and $Zn_{0.25}Cd_{0.75}S_{0.50}Se_{0.50}$ nanoalloy compositions are decreasing respectively as seen in Table 3.1.

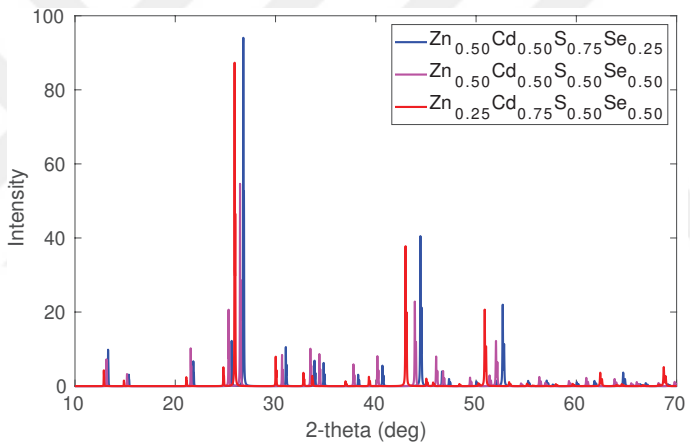

Figure 3.5. The average XRD patterns of $Zn_{0.50}Cd_{0.50}S_{0.75}Se_{0.25}$, $Zn_{0.50}Cd_{0.50}S_{0.50}Se_{0.50}$ and $Zn_{0.25}Cd_{0.75}S_{0.50}Se_{0.50}$ nanoalloy compositions.

The average XDR patterns of these quaternary colloidal alloys are demonstrated in Figure 3.5. All diffraction peaks of the different configurations obtained for the given (x, y) parameters are at the same 2-theta values but at different concentrations. The peak values of alloy compositions are between the peaks of the binary structures (ZnS, CdS, ZnSe and CdSe). The peak positions are consistent with experimental data. The shifts are observed in peak positions when stoichiometry changes are consistent with the changes in the alloy composition parameters. The configuration averages do not lead to a major change in the widths of the peaks. This is considered to change if simulations are performed in larger supercells.

CHAPTER 4

EXCITATION DYNAMICS ON SEMICONDUCTOR SURFACES

In this chapter, we explore excitation dynamics on semiconductor quantum surfaces, which are passivated with organic molecules such as (111) surface of ZnS passivated with oleic acid (OA) molecule. Before going into realistic systems, we present a simplified model to investigate the fundamental properties in the time dependent occupancy in detail in section 4.1. We focus on ZnS nanocluster capped by OA and evalute its the spectral functions for the highest occupied (HOMO) and the lowest unoccupied molecular orbitals (LUMO). In accordance with the results of the spectral functions, we investigate their time dependent occupations. The realistic system studies will be explained in detail in sections 4.2 and 4.3.

4.1. Simplified Model

We use a simplified model to investigate the fundamental features in the time dependent occupancy of a reservoir interacting with frontier molecular orbitals. In the simplified model, the reservoir is considered as the semiconductor surface and molecular orbitals have two states corresponding to the HOMO and the LUMO levels. This model is based on the Fano-Anderson model, which was developed separately by Anderson [58] and Fano [59]. The Fano-Anderson model can be solved exactly. The Hamiltonian was given as [60]

$$H = \epsilon_C b^\dagger b + \sum_k \left[\epsilon_k c_k^\dagger c_k + A_k (c_k^\dagger b + b^\dagger c_k) \right] \tag{4.1}$$

where ϵ_C, b and $b^\dagger$ represent the localized state of fixed energy and operators, respectively. The localized state is called as the impurity. Thus, ϵ_k, c_k and $c_k^\dagger$ represent the the continuous set of states of energy and operators, respectively. The last term stands for the mixing between these kinds of states. We note that the electron-electron interactions are

not considered here. In our simplified model, we consider two states, characterized by energy of states E_1 and E_2, that interacted with a semi-infinite system in Figure 4.1.

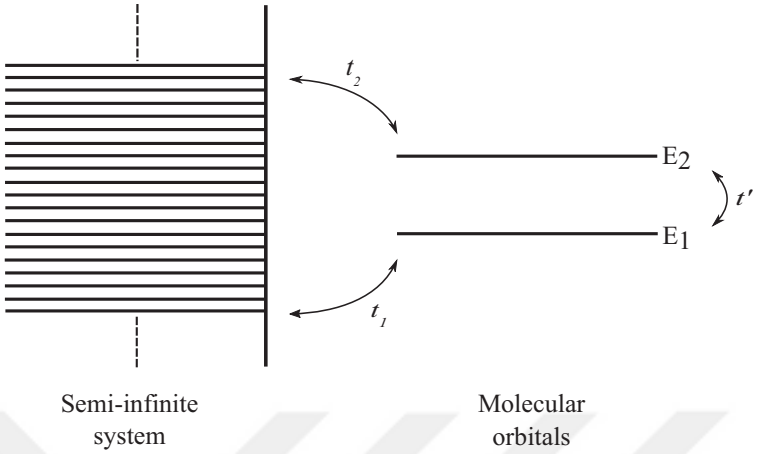

Figure 4.1. Schematic diagram of the simplified model, where t_1 and t_2 are the hopping terms between the semi-infinite system and states $|1\rangle$ and $|2\rangle$, respectively. t' stands for inter-level hopping between $|1\rangle$ and $|2\rangle$.

The total Hamiltonian of the system is an infinitely large matrix because the reservoir is semi-infinite. The effective Hamiltonian for the molecule can be written as

$$\tilde{H}_m(E) = H_m^0 + \Sigma(E), \tag{4.2}$$

where the Hamiltonian of the free molecule H_m^0 is

$$H_m^0 = \begin{pmatrix} E_1 & t' \\ t' & E_2 \end{pmatrix}. \tag{4.3}$$

The effect of semi-infinite system is represented by (2×2) self-energy matrix

$$\Sigma = V\, g_s\, V^\dagger, \tag{4.4}$$

where V refers to the coupling Hamiltonian as $V = \begin{pmatrix} t_1 \\ t_2 \end{pmatrix}$.

Assume that the reservoir consists of a semi-infinite atomic chain, the surface Green's function g_s can be written analytically as [61]

$$g_s = \frac{E}{2t_s^2} - \frac{i}{t_s}\sqrt{1 - \frac{E^2}{4t_s^2}}, \tag{4.5}$$

where t_s is the hopping term between the atoms in the semi-infinite system. Thus, the effective Green's function of the molecule is obtained in matrix form

$$G^m = \left[(E + i\eta)\mathbb{1} - \tilde{H}_m\right]^{-1} \tag{4.6}$$

where $\mathbb{1}$ is the unit matrix of the same size as $\tilde{H}_m$. Inserting Equations 4.3, 4.4 and 4.5 into Equation 4.6 gives the Green's function of the system,

$$G^m = \left[(E + i\eta)\mathbb{1} - \begin{pmatrix} E_1 & t' \\ t' & E_2 \end{pmatrix} - \begin{pmatrix} t_1^2 g_s & t_1 t_2 g_s \\ t_2 t_1 g_s & t_2^2 g_s \end{pmatrix}\right]^{-1}. \tag{4.7}$$

Spectral function is obtained by

$$A(E) = -\frac{1}{\pi}\mathrm{Im}\left[G^m\right], \tag{4.8}$$

and the trace of the spectral function gives the total spectrum, also known as the density of states. The time dependent occupancy can be written in terms of the spectral functions as

$$\langle n_j(t)\rangle = \langle n_j(0)\rangle \left| \int dE\, A_{jj}(E) e^{-\frac{iEt}{\hbar}} \right|^2. \tag{4.9}$$

If t' is different from zero, we need to apply a unitary transformation in order to examine the time dependent occupations of the excitations.

The total Hamiltonian H is described as

$$H = \begin{pmatrix} H_m^0 & V \\ V^\dagger & H_r \end{pmatrix}, \tag{4.10}$$

where the term H_r represents the semi-infinite reservoir. Denoting the matrix that diagonalizes H_m^0 as u, one writes

$$U = \begin{pmatrix} u & 0 \\ 0 & \mathbb{1} \end{pmatrix}, \tag{4.11}$$

and

$$H' = U^\dagger \, H \, U. \tag{4.12}$$

By using the Equation 4.10 in the Equation 4.12 we derive

$$\begin{aligned} H' &= \begin{pmatrix} u^\dagger & 0 \\ 0 & \mathbb{1} \end{pmatrix} \begin{pmatrix} H_m^0 & V \\ V^\dagger & H_r \end{pmatrix} \begin{pmatrix} u & 0 \\ 0 & \mathbb{1} \end{pmatrix} \\ &= \begin{pmatrix} u^\dagger \, H_m^0 & u^\dagger \, V \\ V^\dagger & H_r \end{pmatrix} \begin{pmatrix} u & 0 \\ 0 & \mathbb{1} \end{pmatrix} \\ &= \begin{pmatrix} u^\dagger \, H_m^0 \, u & u^\dagger \, V \\ V^\dagger \, u & H_r \end{pmatrix}. \end{aligned} \tag{4.13}$$

After applying the unitary transformation, the effects of semi-infinite system Σ' can be obtained as (2×2) self-energy matrices,

$$\begin{aligned} \Sigma' =& u^\dagger \, V \, g_s \, V^\dagger \, u, \\ =& u^\dagger \, \Sigma \, u. \end{aligned} \tag{4.14}$$

4.1.1. Spectra of HOMO and LUMO

In the following, we present our results for the simplified model for two different cases; $t' = 0$ and $t' \neq 0$. In order to be able to explain the time dependent occupancies, we need to understand the behaviors of the spectral functions. In Figures 4.2 and 4.3 the spectral functions (solid curves) and the densities of states (dashed curve) are plotted, which are obtained using Green's functions as explained above. We used the following set of values for (t_1, t_2) as ($t_1 = 0.10$, $t_2 = 0.10$), ($t_1 = 0.10$, $t_2 = 0.25$), ($t_1 = 0.30$, $t_2 = 0.30$) and ($t_1 = 0.30$, $t_2 = 0.45$). We also consider the states $|1\rangle$ and $|2\rangle$ to have energies with a narrow splitting ($E_1 = 0.20$, $E_2 = 0.25$) and a relatively wider splitting ($E_1 = 0.20$, $E_2 = -0.20$).

A few reminders considering the spectral function are in order here. The molecular levels are shifted and broadened when they are coupled to the reservoir. The shift is larger and the broadening is wider when the coupling is stronger. If the peaks are isolated, the total spectrum resembles a collection of independent levels. Otherwise, one expects features originating from multi-level mixing.

Densities of states and spectral functions in the absence of inter-level hopping between states $|1\rangle$ and $|2\rangle$ ($t' = 0$) are given in Figure 4.2. The spectra are not changed considerably when the overlap is negligible. We can see that, when there is appreciable overlap the Lorentzian is distorted and a dip is observed coinciding with the neighboring resonance.

Figures 4.2(a,c) demonstrate the spectra for small hopping terms. We see that the Lorentzians overlap and their shapes are distorted. In Figure 4.2(b,d), we can see that the shift and the broadening increase as hopping term t_2 increases. When $t' = 0$, the peaks tend to stay away from each other. In fact when $t' = 0$, there exist a narrowing effect on the molecular levels. We will see the effets of these situations on time dependent occupancies. For example, if the hopping terms equal each other ($t_1 = t_2$) and the spectra have energies $E_1 = 0.20$ and $E_2 = -0.20$, the level spectra are symmetric as in Figures 4.2(c,g).

When the hopping terms are increased, e.g. Figure 4.2(e), the level spectra have appreciable overlap, the dressed state have narrow peaks and the Lorentzian shapes are extremely distorted. Figure 4.2(f) shows the difference between Lorentzian widths which are increasing since the hopping term t_2 is increased in that case. In Figure 4.2(h), the spectrum of E_2 level is distorted by the spectrum of E_1 level. It is seen that from the peak corresponding to the spectrum of E_2 level to the right side rapidly decays to zero but it has

a longer tail at the left hand side. In addition to this, it was observed that the neighboring level makes a dip where the spectrum is maximized.

Figure 4.3 demonstrates spectral functions and densities of states that allows interaction between the frontier molecular orbitals, which affects occupations. We see that the Lorentzians overlap and their shapes are distorted. We will observe that this affects the time dependent occupancy dramatically. When the inter-level hopping is different from zero, level spectra are not symmetric even if the hopping terms equal to each other ($t_1 = t_2$) and the spectra have energies $E_1 = 0.20$ and $E_2 = -0.20$ as seen in Figures 4.3(c,g).

Figures 4.3(a,c) demonstrate the spectra for the same and small hopping terms. We can observe that the dressed states have a narrowing peak and each spectrum level have two peaks on their bare states. Therefore, Lorentzians overlap and their shapes are extremely distorted. Figures 4.3(b,d) show that the shift and the broadening increase due to the increase in the hopping term t_2, also we can clearly see the different Lorentzian widths along the spectra. We continue analyzing by increasing the values of hopping terms.

Figure 4.3(e) shows the spectra for the same hopping terms but the energy band gap is narrower. The dressed states consist of two peaks. Morever, when t_2 hopping term is increased, the spectrum of E_2 level is distorted by the spectrum of E_1 level as seen in Figure 4.3(f). It is observed that the spectrum of E_2 level makes a dip where the spectrum of E_1 level has one peak around its bare state. The Lorentzian is distorted with increasing the broadening for the spectrum of E_1 level. The spectrum of E_2 level also is observed to having declining peaks and the broadening increases.

Figure 4.3(g) shows the hoping terms are the same and the energy band gap is wider, the level spectra do not have the same behaviors compared to $t' = 0$ on their bare states. The spectrum of E_1 level has a shoulder at the left hand side; however the spectrum of E_2 level makes a dip around zero and then we see a shoulder at the right hand side. When t_2 hopping term is increased, the broadening increases and the dressed state has two peaks for the spectrum of E_1 level, and also the spectrum of E_2 level maintains the effect of the shoulder at the right hand side as seen in Figure 4.3(h). We will see that these shoulders affect their time dependent occupations.

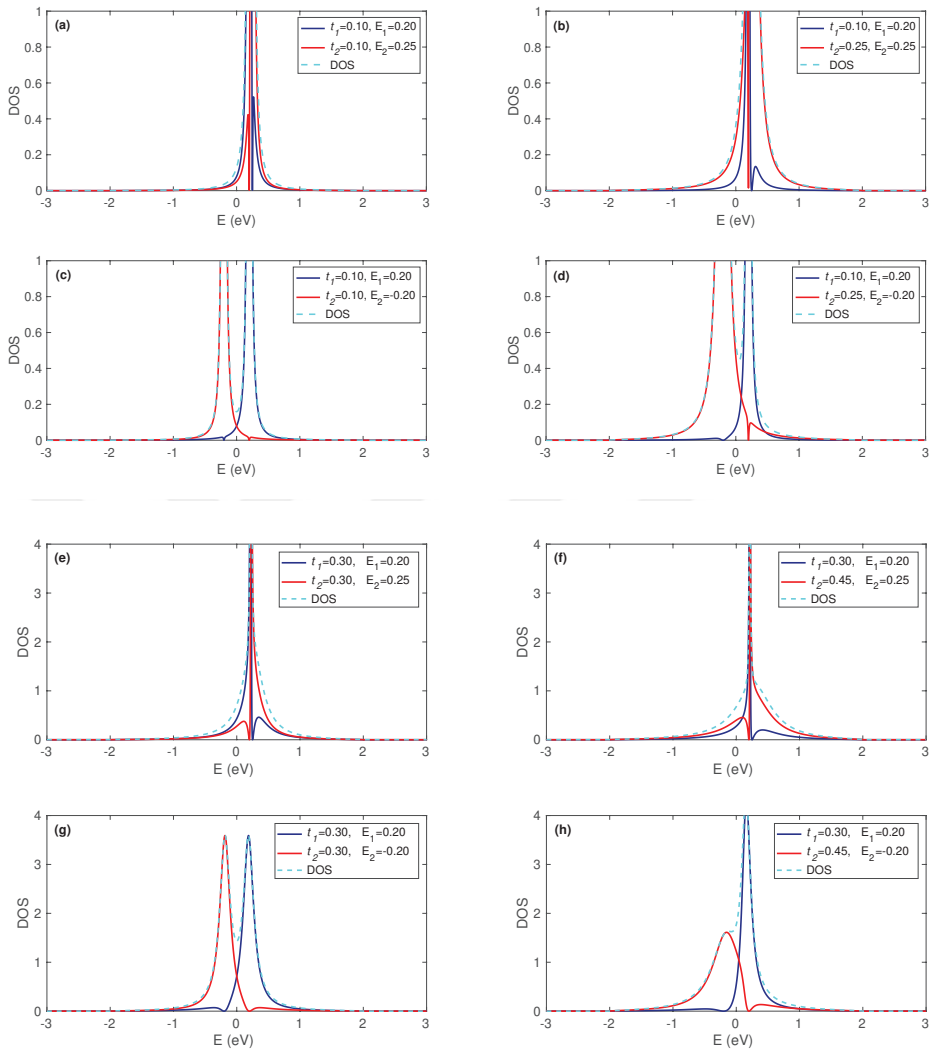

Figure 4.2. Spectra of frontier molecular orbitals. In the left column (a, c, e, g) and in the right column (b, d, f, h) are taken $t_1 = t_2$ and $t_1 \neq t_2$, respectively. In the first and third row, HOMO and LUMO energy levels are chosen as narrow, in second and fourth row, they are chosen as wide. The inter-level hopping term between $|1\rangle$ and $|2\rangle$ is chosen to be t'=0.

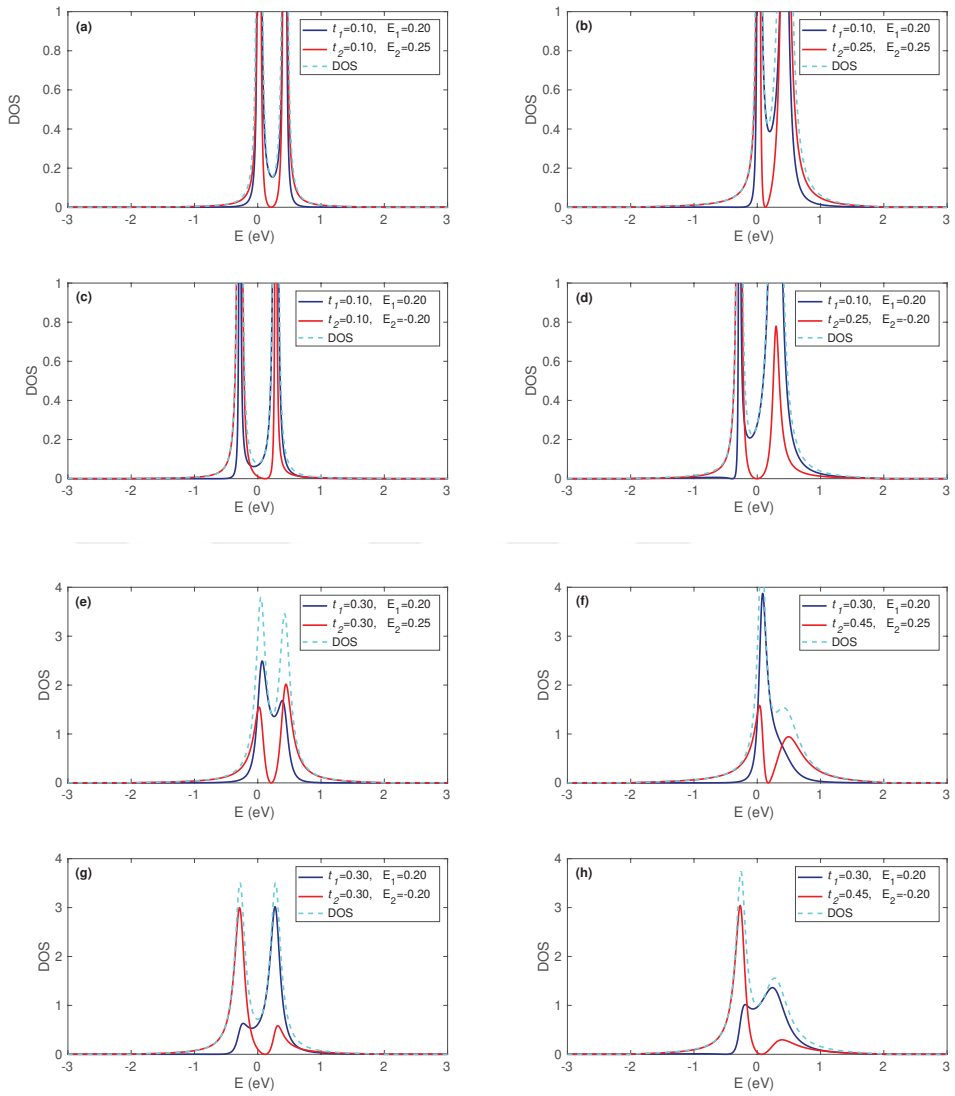

Figure 4.3. Spectra of frontier molecular orbitals. In the left column (a, c, e, g) and in the right column (b, d, f, h) are taken $t_1 = t_2$ and $t_1 \neq t_2$, respectively. In the first and third row, HOMO and LUMO energy levels are chosen as narrow, in second and fourth row, they are chosen as wide. The inter-level hopping term between $|1\rangle$ and $|2\rangle$ is chosen to be t'=0.20

4.1.2. The Time Dependent Occupancy of HOMO and LUMO

Two situations are investigated within the simplified model. First we start from the spectral functions with non-interacting inter-level hopping term ($t' = 0$). We see how the spectra of frontier molecular orbitals have energies with a narrow and wider splitting (E_1,E_2) evolve under different and same parameters for the hopping terms correspond to the semi-infinite system and molecular levels (t_1, t_2). Second we start from the spectral functions with interacting inter-level hopping term ($t' = 0.20$) and see how the spectra of frontier molecular orbitals have energies with a narrow and wider splitting (E_1,E_2) evolve under different and same parameters for the hopping terms (t_1, t_2). Finally, according to our spectral functions, we can start analyzing the time dependent occupations.

Figure 4.4 shows the time dependent occupancies which are estimated using the calculation of spectral functions with the inter-level hopping $t' = 0$. In Figures 4.4(a,e), firstly, we can observe that occupations overlap. Then the two values start to drift away from each other. To examine this result, we investigate the spectra in Figures 4.2(a,e), we can see that their spectra have narrowing effect on the molecular levels and the dressed state has antiresonance where the neighbouring level gives a peak. Therefore, the effect of the antiresonance leads to fluctuations during decay and then the overlap separates from each other.

Figures 4.4(c,g) demonstrate that the occupations have the same behavior because their spectra show the same behavior around their bare states. t_1 hopping term is kept constant while t_2 hopping term is changed, we observe that oscillations decay with different ratios. In Figure 4.4(d), the occupation of E_2 level decays faster than the occupation of E_1 level due to the wider Lorentzian width. Figure 4.4(f) shows the occupations of states decay with different ratios due to the different Lorentzian widths; however they behave stable from 0.05 to 0.2 picoseconds. In Figure 4.4(h), the occupation of E_2 level decays faster because its Lorentzian width is wider than the occupation of E_1 level.

We also compare our calculations with uncertainty relations. According to the Heisenberg uncertainty relations, the energy uncertainy ΔE is expressed as

$$\Delta E \; \Delta t \geq \frac{\hbar}{2} \tag{4.15}$$

where Δt is the particle lifetime as the uncertainty in time. The energy uncertainty is described as the width of the Lorentzian distribution at half maximum. For example, in

Figure 4.4(c), the half life is measured to be 0.14 picoseconds for each occupation and their Lorentzian widths read 0.015 eV. Moreover, in Figure 4.4(d), the half life for the spectrum of E_1 level is 0.15 picoseconds and the half life for the occupation of E_2 level is 0.02 picoseconds with their Lorentzian widths are 0.014 eV and 0.10 eV, respectively. The occupations are found to consistent with the predicted values by the uncertainty relations using Equation 4.15 for the simplified model.

Figure 4.5 demonstrates the time dependent occupancies which are estimated using the calculation of spectral functions with the inter-level hopping $t' = 0.20$. Figure 4.5 shows that fluctuations and oscillations are stronger than Figure 4.4 owing to the interaction between molecular levels. When hopping terms have low values, the fluctuations of occupations become more periodic. When t_1 and t_2 hopping terms are increased, it is observed that the oscillations are decreasing more rapidly and the occupations of the level spectra decay with different rates. We also observe that the decay of occupations gives drop retardations as hopping terms increase. Figure 4.5(a,c) show that the fluctuations and oscillations are more periodically decaying because their spectra have two peaks on bare states. We keep t_1 hopping term constant while changing t_2 hopping term and investigate dependence of decay of t_1 hopping term on the separation from each other. Figure 4.5(b) shows t_2 hopping term is shifting according to t_1 hopping term. The occupations of the molecular levels split during decay in Figure 4.5(d). When t_1 and t_2 hopping terms increase, it is seen that oscillations shift and fluctuations are effectively destroyed. We obtain that oscillations decay more rapidly in Figure 4.5(e,g). Figure 4.5(e) demonstrates the occupation for the spectrum of E_2 level decays faster than the occupation for the spectrum of E_1 level; however we can observe that pronounced shoulder is visible on occupations of molecular levels. Figure 4.5(g) shows for the same hopping term and the energy band gap is wider. If the inter-level hopping term t' is not available, both occupations have the same behavior. As molecular level mixing at the inter-level hopping term $t' = 0.20$, we also investigate the behavior of spectral functions in Figure 4.3(g), molecular levels have shoulders. These result in fluctuations during decay as remnants of the effect of the shoulders. We continue analyzing the case where t_1 hopping term is kept constant while t_2 hopping term is increased. Figure 4.5(f) shows that the occupation of E_2 level decays faster than the occupation of E_1 level. We can interpretate their occupations to investigate their spectra in Figure 4.3(f), and it is observed that the behavior of the spectrum of E_2 level has the antiresonance and shoulders. Therefore, these lead to fluctuations during decay particularly the effect on the occupation of E_2 level is observed. We observe that the effects of shoulders in spectra are still visible in the occupations in Figure 4.5(h).

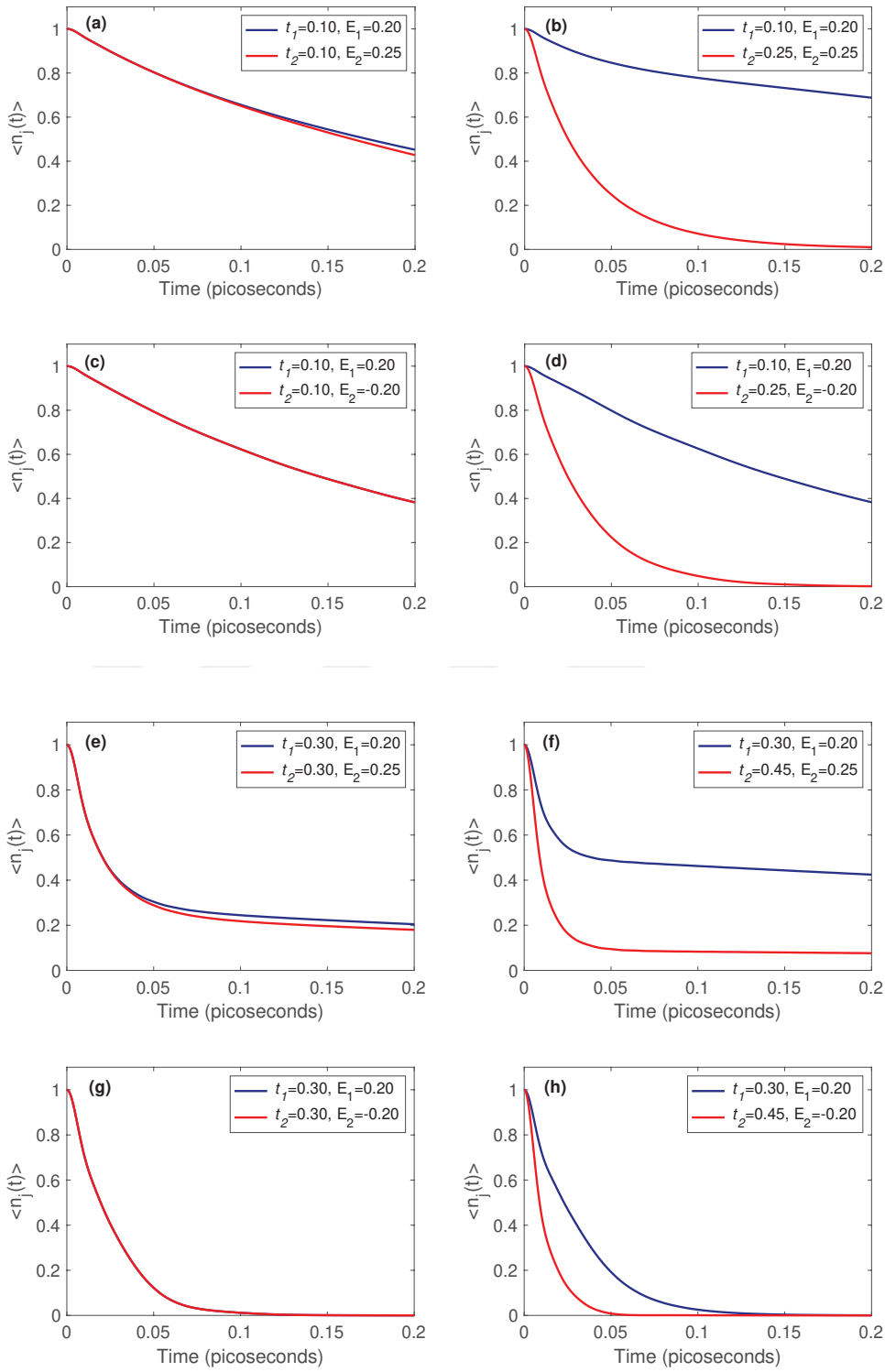

Figure 4.4. The time dependent occupancy of frontier molecular orbitals. In the left column (a, c, e, g) and in the right column (b, d, f, h) are taken t_1=t_2 and $t_1 \neq t_2$, respectively. In the first and third row, HOMO and LUMO energy levels are chosen as narrow, in second and fourth row, they are chosen as wide. The inter-level hopping term between $|1\rangle$ and $|2\rangle$ is chosen to be t'=0.

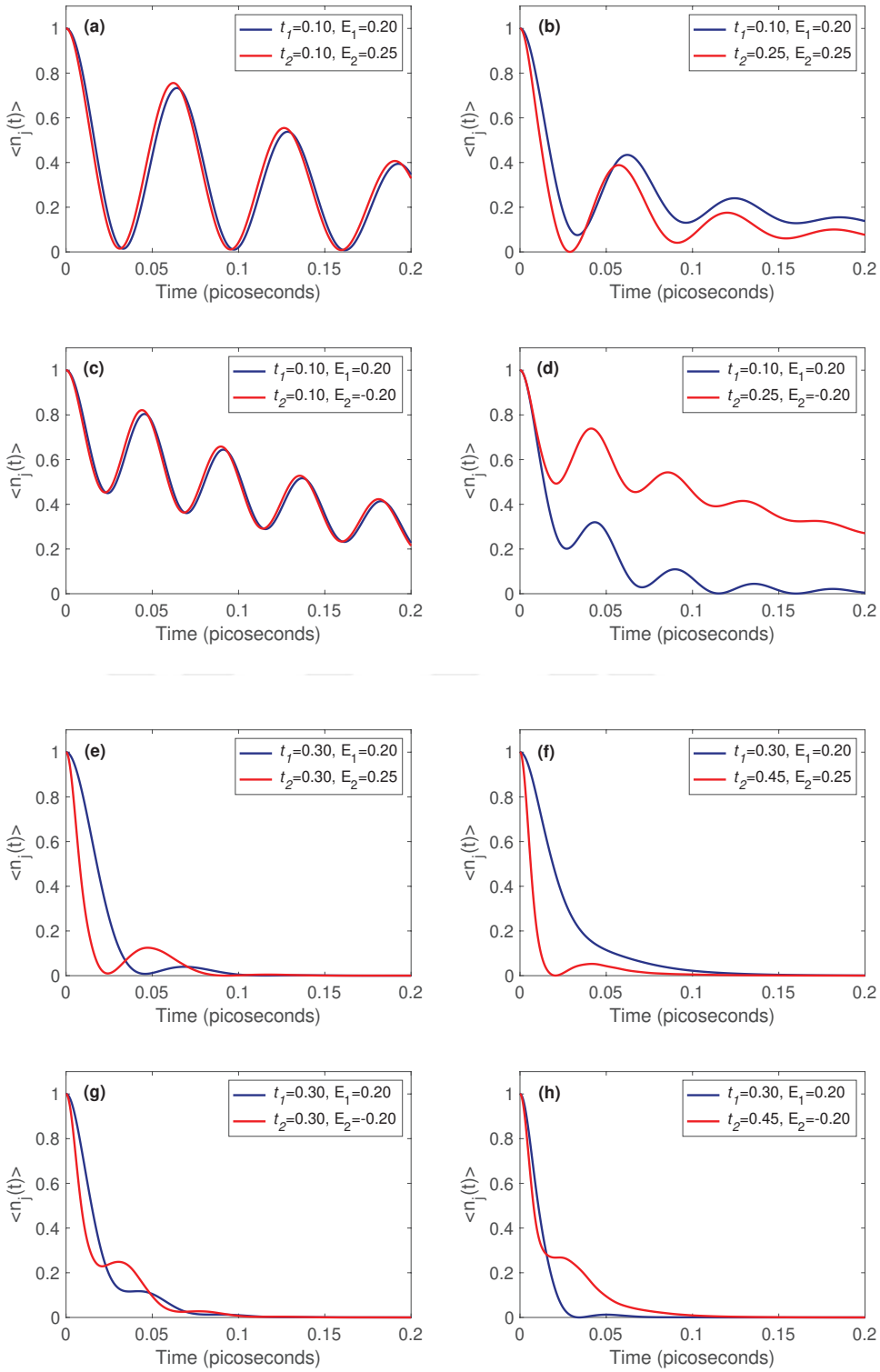

Figure 4.5. The time dependent occupancy of frontier molecular orbitals. In the left column (a, c, e, g) and in the right column (b, d, f, h) are taken t_1=t_2 and $t_1 \neq t_2$, respectively. In the first and third row, HOMO and LUMO energy levels are chosen as narrow, in second and fourth row, they are chosen as wide. The inter-level hopping term between $|1\rangle$ and $|2\rangle$ is chosen to be t'=0.20.

4.2. ZnS (111) Surface Passivation with Oleic Acid

In the experiments, quantum dots are usually passivated with oleic acid. Figure 4.6 demonstrates the oleic acid used in the experiments. Oleic acid is a monounsaturated fatty acid molecule and the formula of oleic acid is $CH_3(CH_2)_7CH{=}CH\text{-}(CH_2)_7COOH$, which has one double bond between the carbons. The cis configuration and trans configuration of the oleic acid are available. In Figure 4.6, (a) shows the cis configuration of oleic acid and (b) shows the trans configuration of oleic acid.

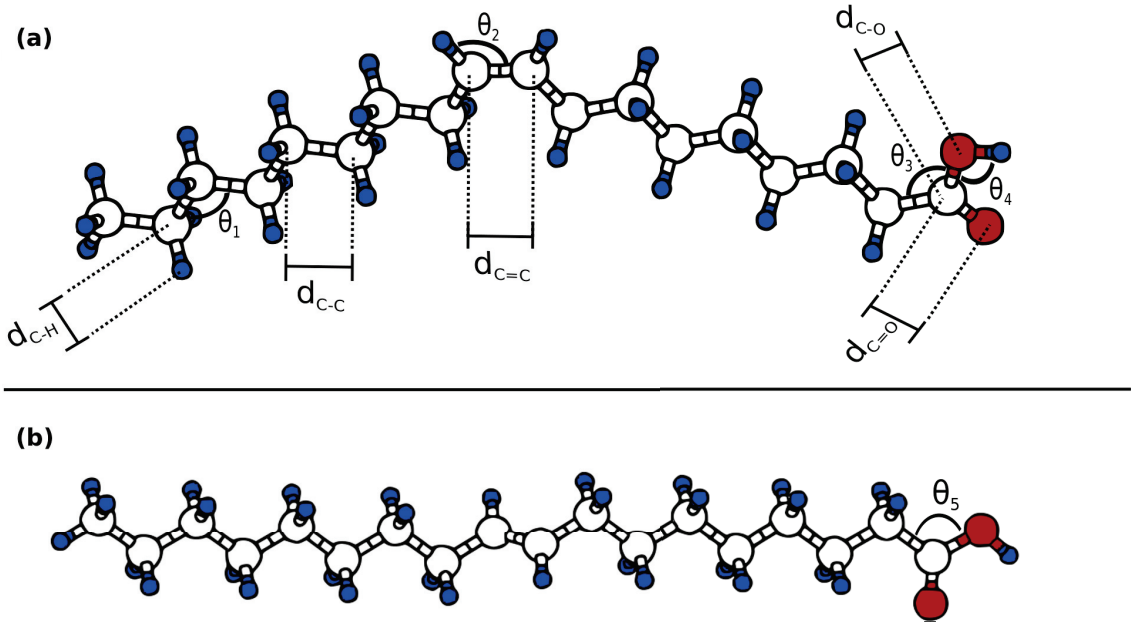

Figure 4.6. Oleic acid structure. (a) The structure of cis-oleic acid. (b) The structure of trans-oleic acid. White, blue and red colors represent C, H and O atoms, respectively. d is the bond length and θ is the bond angle. Related structural parameters are detailed in Table 4.1.

The structures of trans and cis configurations for oleic acid are constructed by using the values of the bond length and the bond angle in Table 4.1, where $d_{C=C}$ and $d_{C=O}$ represent the double bond length between carbon-carbon and carbon-oxygen atoms, respectively. And then, the bond angle (θ_3,θ_4) is determinated according to the bond angles of the acetic acid. In the theoretical calculations, the structural optimizations are carried out with density functional theory based tight binding (DFTB) method based on self-consistency as implemented in DFTB+ package.

The atomic positions in the structures are optimized so that the maximum force is less than 0.01 eV /Å and the convergence criterion for total energy set to 10^{-4} Hartree for all cases. For trans and cis configurations of oleic acid, the charge mixing method is Broyden with 1.5 as the mixing parameter. Additionally, for passivation configurations, the charge mixing method is Anderson with 0.05 as the mixing parameter. As a result of calculations, total energy values are found to be -1372.83 eV for the cis configuration of oleic acid, while it reads -1372.88 eV for the trans configuration of oleic acid. Total energy values are observed to be close to each other. Therefore, in our studies, we have mostly designed using the structures of trans configuration oleic acid while we have investigated excitation dynamics of passivation of ZnS (111) surface with oleic acid.

Table 4.1. Structural properties of the trans and cis configurations of oleic acid. Bond length ($d_{\text{C-H}}$, $d_{\text{C-C}}$, $d_{\text{C=C}}$, $d_{\text{C-O}}$, $d_{\text{C=O}}$) and bond angle (θ_1, θ_2, θ_3, θ_4, θ_5). See Figure 4.6 for length and angle references.

Bond length (Å)		Bond angle (deg)	
C-H ($d_{\text{C-H}}$)	1.09	C-C-C (θ_1)	109.50
C-C ($d_{\text{C-C}}$)	1.54	H-C=C (θ_2)	119.99
C=C ($d_{\text{C=C}}$)	1.34	C-C-O (θ_3)	119.99
C-O ($d_{\text{C-O}}$)	1.43	H-O-C (θ_4)	106.00
C=O ($d_{\text{C=O}}$)	1.21	C-C-O (θ_5)	112.29

Figure 4.7(a) demonstrates the unit cell of oleic acid (OA) on the ZnS (111) surface in which there are 145 atoms, containing 44 S, 44 Zn, 18 C, 37 H and 2 O atoms. H atoms added to S atoms in order to passivate the dangling bonds. Oleic acid molecule looses one hydrogen atom in its carboxyl functional group (COOH) and oleic acid (OA) molecule convert to oleate (OA^-) molecule, which then binds to ZnS surface. In order to investigate surface excitations in a system, it is necessary to assess the Hamiltonian and the overlap matrices. The structure was separated into layers for using these matrices in Green's function calculations. The unit cell is partitioned as four layers. The first three layer are fixed while the fourth layer is relaxed. The thickness of the layers were determined according to overlaps of neighboring atomic orbitals, and layer thickness is set to 10 Å. The determination of the layer thickness is given in detail in the Appendix A. A sufficiently large vacuum spacing of at least 19.25 Å is inserted in z direction. $3 \times 3 \times 1$

supercell is constructed from the unit cell of an oleate molecule on the ZnS (111) surface. This supercell is then separated into four parts in the z direction (layer 1, 2, 3,4) in Figure 4.7(b), and into nine areas in the xy-plane (A, B, C, D, E, F, G, H, I) in Figure 4.7(c).

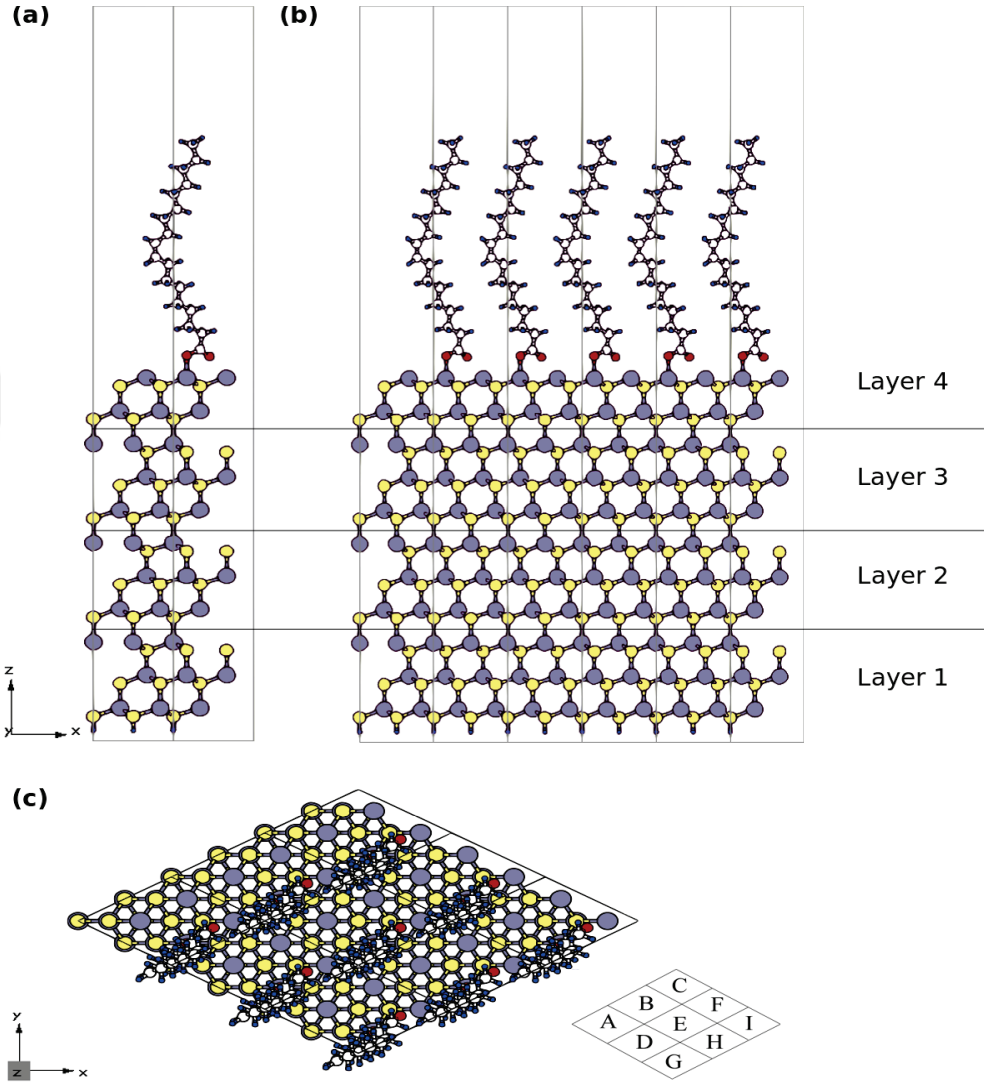

Figure 4.7. (a) Unit cell of OA^- molecule on the ZnS (111) surface in z direction. Layer 1, 2, 3 are fixed and layer 4 is relaxed. $3 \times 3 \times 1$ supercell from unit cell (b) in z direction and (c) in the xy plane. (b) The supercell is divided into 4 layers (1, 2, 3, 4). (c) On the right, a simplified z-view schematic diagram of supercell divided into 9 areas (A, B, C, D, E, F, G, H, I). Zn, gray; S, yellow; C, white; H, blue; O, red.

4.3. Dynamics on ZnS Surface

In this section, our methodology, the passivation configurations and the numerical results for realistic systems will be presented in detail in the following subsections.

4.3.1. Hamiltonian and Overlap Matrices

We simulate a semi-infinite ZnS crystal, terminated at its 111 surface and passivated with oleic acid (OA). For obtaining the Hamiltonian and overlap matrices, a finite layer of ZnS is used, which is passivated using hydrogen atoms at the opposite side (see Figure 4.8). Figure 4.8(a) illustrates that there are surface layer, ZnS layer and termination layer. The surface layer contains the free molecule and a part of the surface, ZnS layer involves only bulk ZnS layers and the termination layer is passivated using hydrogen atoms. Periodic boundary conditions are imposed in the xy-plane. Namely, the shaded area in Figure 4.8(b) is repeated to form a $3 \times 3 \times 1$ supercell in the xy-plane.

In order to start the calculations, the Hamitonian and overlap matrices are extracted by performing geometry optimization using DFTB method. In the system, we need to solve the generalized eigenvalue equation in order to obtain the energy eigenvalues and wavefunctions:

$$\tilde{H}\tilde{\psi} = E\tilde{S}\tilde{\psi}, \tag{4.16}$$

where $\tilde{H}$ is the Hamiltonian matrix and $\tilde{S}$ is the corresponding overlap matrix. DFTB makes use of non-orthogonal basis sets formed from atomic orbitals. We distinguish operators and wavefunctions written in non-orthogonal basis with a tilde as $\tilde{H}$, $\tilde{S}$ and $\tilde{\psi}$. The Hamiltonian and overlap matrix elements are separated according to the partitioning scheme in Figure 4.8. They can be organized into four blocks

$$\tilde{H} = \begin{pmatrix} \tilde{H}_{SS} & \tilde{H}_{SB} \\ \tilde{H}_{SB}^{\dagger} & \tilde{H}_{BB} \end{pmatrix} \quad \tilde{S} = \begin{pmatrix} \tilde{S}_{SS} & \tilde{S}_{SB} \\ \tilde{S}_{SB}^{\dagger} & \tilde{S}_{BB} \end{pmatrix} \tag{4.17}$$

where the subscripts SS and BB correspond to the surface layer and ZnS layer respectively, and the off-diagonal terms correspond to the couplings between these layers.

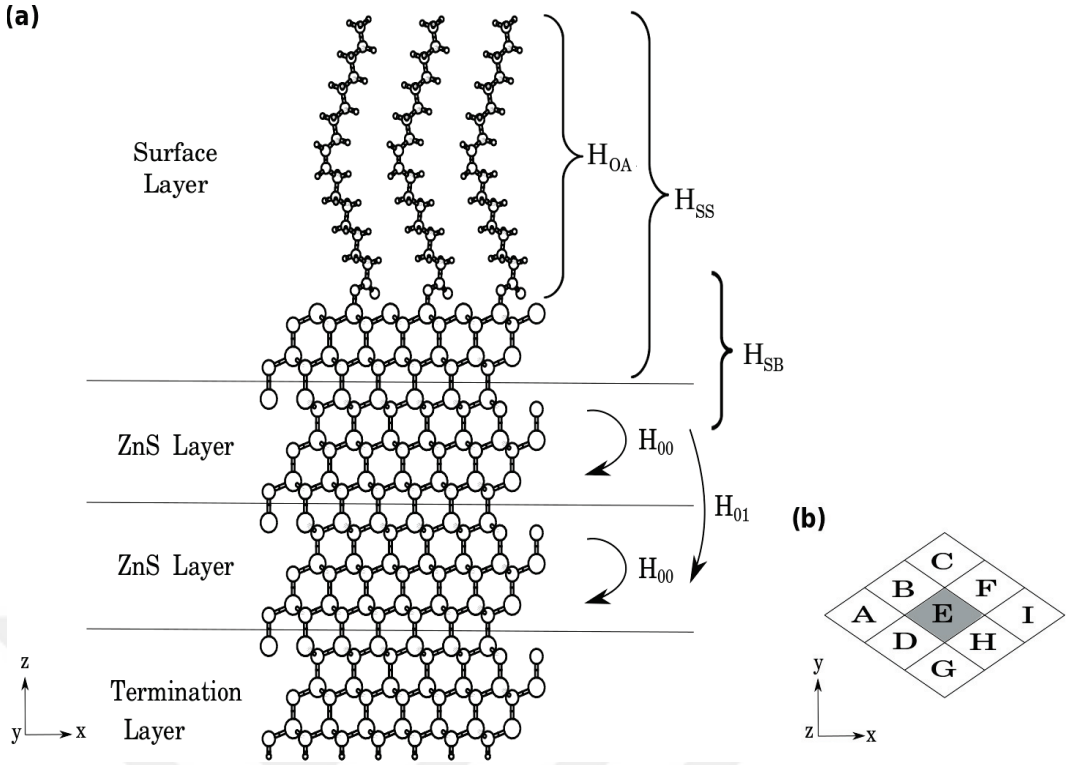

Figure 4.8. Schematic passivation configuration for oleate (OA^-) ligand on the ZnS (111) surface (a) in z direction and (b) in the xy-plane. H_{OA} refers the Hamiltonian for OA^- ligand on the surface. H_{SS} contains matrix elements between the surface layer and H_{SB} involves coupling between the surface layer and ZnS layer. H_{00} and H_{01} are the Hamiltonian matrix elements the ZnS layer and between ZnS layers, respectively.

The Hamiltonian and the corresponding overlap matrix elements can be constructed using periodic boundary conditions where $\vec{R}_{E\alpha}$ is the vector joining cell E to cell α and $\vec{k}$ is the wave vector. $\tilde{H}_{SS}$ is defined by

$$\tilde{H}_{SS} = \tilde{H}_{SS}^{EE} e^{i\vec{k}\cdot\vec{R}_{EE}} + \sum_{\alpha} \sum_{\vec{k}} \tilde{H}_{SS}^{E\alpha} e^{i\vec{k}\cdot\vec{R}_{E\alpha}}. \tag{4.18}$$

Here, α shows the repeated cells in the xy-plane (A, B, C, D, F, G, H, I) and only the $\vec{k} = 0$ components are used. Consequently, $\tilde{H}_{SB}$ can be written as

$$\tilde{H}_{SB} = \tilde{H}_{SB}^{EE} + \sum_{\alpha} \tilde{H}_{SB}^{E\alpha}. \tag{4.19}$$

$\tilde{H}_{BB}$ can be written in bipartite matrix form as

$$\tilde{H}_{BB} = \begin{pmatrix} \tilde{H}_{00} & \tilde{H}_{01} \\ \tilde{H}_{01}^{\dagger} & \tilde{H}_{00} \end{pmatrix} \tag{4.20}$$

where

$$\tilde{H}_{00} = \tilde{H}_{00}^{EE} + \sum_{\alpha} \tilde{H}_{00}^{E\alpha}, \tag{4.21}$$

$$\tilde{H}_{01} = \tilde{H}_{01}^{EE} + \sum_{\alpha} \tilde{H}_{01}^{E\alpha}. \tag{4.22}$$

The overlap matrix can also be written in the same way as the Hamiltonian matrix. Additionally, the Hamiltonian and overlap parts, which represent coupling of non-neighbouring parts are checked if they are zero. This is a requirement for Green's function calculations. To sum up, all matrix parts are checked if the layer matrices were taken correctly.

In our calculations we prefer to use orthogonal basis sets. Hence, we first apply a unitary transformation R that orthogonalizes $\tilde{H}_{SS}$ and leaves $\tilde{H}_{BB}$ untouched. Multiplication of both sides with R gives

$$R\tilde{H}\tilde{\psi} = ER\tilde{S}\tilde{\psi} \tag{4.23}$$

where $R = \begin{pmatrix} \tilde{S}_{SS}^{-1/2} & 0 \\ 0 & \mathbb{1} \end{pmatrix}$ and using $1 = RR^{-1}$, one can write

$$R\tilde{H}RR^{-1}\tilde{\psi} = ER\tilde{S}RR^{-1}\tilde{\psi}. \tag{4.24}$$

We can put the above equation in a more compact form

$$H\psi = ES\psi \tag{4.25}$$

where H, S and ψ are defined by $H = R\tilde{H}R,\ S = R\tilde{S}R$ and $\psi = R^{-1}\tilde{\psi}$ which are now written in the hybrid basis of orthogonal and non-orthogonal orbitals.

We can write

$$
\begin{aligned}
H &= R\,\tilde{H}\,R \\
&= \begin{pmatrix} \tilde{S}_{SS}^{-1/2} & 0 \\ 0 & \mathbb{1} \end{pmatrix} \begin{pmatrix} \tilde{H}_{SS} & \tilde{H}_{SB} \\ \tilde{H}_{SB}^{\dagger} & \tilde{H}_{BB} \end{pmatrix} \begin{pmatrix} \tilde{S}_{SS}^{-1/2} & 0 \\ 0 & \mathbb{1} \end{pmatrix} \\
&= \begin{pmatrix} \tilde{S}_{SS}^{-1/2}\tilde{H}_{SS} & \tilde{S}_{SS}^{-1/2}\tilde{H}_{SB} \\ \tilde{H}_{SB}^{\dagger} & \tilde{H}_{BB} \end{pmatrix} \begin{pmatrix} \tilde{S}_{SS}^{-1/2} & 0 \\ 0 & \mathbb{1} \end{pmatrix} \\
&= \begin{pmatrix} \tilde{S}_{SS}^{-1/2}\tilde{H}_{SS}\tilde{S}_{SS}^{-1/2} & \tilde{S}_{SS}^{-1/2}\tilde{H}_{SB} \\ \tilde{H}_{SB}^{\dagger}\tilde{S}_{SS}^{-1/2} & \tilde{H}_{BB} \end{pmatrix}
\end{aligned} \tag{4.26}
$$

where

$$
\begin{aligned}
H_{SS} &= \tilde{S}_{SS}^{-1/2}\tilde{H}_{SS}\tilde{S}_{SS}^{-1/2} \\
H_{SB} &= \tilde{S}_{SS}^{-1/2}\tilde{H}_{SB} \\
H_{SB}^{\dagger} &= \tilde{H}_{SB}^{\dagger}\tilde{S}_{SS}^{-1/2} \\
H_{BB} &= \tilde{H}_{BB}.
\end{aligned} \tag{4.27}
$$

S can be also written in the same way. After this rearrangement, we need to apply one more unitary transformation U that diagonalizes H_{SS}. We acquire the molecular orbitals of the surface part of the Hamiltonian, so that the first block of Equation 4.26 becomes diagonal as shown Equation 4.32. But the point is that diagonal elements are the eigenvalues of $\tilde{H}_{OA}$. U can be written as

$$
U = \begin{pmatrix} u & 0 \\ 0 & \mathbb{1} \end{pmatrix} \tag{4.28}
$$

and applying the unitary transformation in Equation 4.25

$$
U^{\dagger}HUU^{\dagger}\psi = EU^{\dagger}SUU^{\dagger}\psi. \tag{4.29}
$$

We can show that

$$h\varphi = Es\varphi \tag{4.30}$$

where h, s and φ

$$h = U^{\dagger}HU,\ s = U^{\dagger}SU \ \text{ and } \ \varphi = U^{\dagger}\psi. \tag{4.31}$$

From now on, we denote the diagonal matrices with lower case. We can write

$$\begin{aligned} h &= U^{\dagger}\ H\ U \\ &= \begin{pmatrix} u^{\dagger} & 0 \\ 0 & \mathbb{1} \end{pmatrix} \begin{pmatrix} H_{SS} & H_{SB} \\ H_{SB}^{\dagger} & H_{BB} \end{pmatrix} \begin{pmatrix} u & 0 \\ 0 & \mathbb{1} \end{pmatrix} \\ &= \begin{pmatrix} u^{\dagger}H_{SS} & u^{\dagger}H_{SB} \\ H_{SB}^{\dagger} & H_{BB} \end{pmatrix} \begin{pmatrix} u & 0 \\ 0 & \mathbb{1} \end{pmatrix} \\ &= \begin{pmatrix} u^{\dagger}H_{SS}u & u^{\dagger}H_{SB} \\ H_{SB}^{\dagger}u & H_{BB} \end{pmatrix} \end{aligned} \tag{4.32}$$

where

$$\begin{aligned} h_{SS} &= u^{\dagger}\tilde{S}_{SS}^{-1/2}\tilde{H}_{SS}\tilde{S}_{SS}^{-1/2}u \\ h_{SB} &= u^{\dagger}\tilde{S}_{SS}^{-1/2}\tilde{H}_{SB} \\ h_{SB}^{\dagger} &= \tilde{H}_{SB}^{\dagger}\tilde{S}_{SS}^{-1/2}u \\ h_{BB} &= \tilde{H}_{BB}. \end{aligned} \tag{4.33}$$

Similarly, we can write to overlap matrix s. The Green's function of the whole system is defined by

$$(\epsilon s - h)G = \mathbb{1} \tag{4.34}$$

where $\epsilon = (E + i\eta)$, E is the energy variable, $i\eta$ is an imaginary quantity and $\mathbb{1}$ is the identity matrix. The Green's function can be partitioned as

$$\begin{pmatrix} \epsilon s_{SS} - h_{SS} & \epsilon s_{SB} - h_{SB} \\ \epsilon s_{SB}^{\dagger} - h_{SB}^{\dagger} & \epsilon s_{BB} - h_{BB} \end{pmatrix} \begin{pmatrix} G_{SS} & G_{SB} \\ G_{BS} & G_{BB} \end{pmatrix} = \mathbb{1}. \tag{4.35}$$

Performing the first column of the identity matrix using right-hand side, the identities arrive at the following relations

$$(\epsilon s_{SS} - h_{SS})G_{SS} + (\epsilon s_{SB} - h_{SB})G_{BS} = 1 \tag{4.36}$$

$$(\epsilon s_{SB}^{\dagger} - h_{SB}^{\dagger})G_{SS} + (\epsilon s_{BB} - h_{BB})G_{BS} = 0. \tag{4.37}$$

In the above relations, we now write the off-diagonal terms of the Green's function G_{BS} in terms of G_{SS} using Equation 4.37 as

$$G_{BS} = -(\epsilon s_{BB} - h_{BB})^{-1}(\epsilon s_{SB}^{\dagger} - h_{SB}^{\dagger})G_{SS}. \tag{4.38}$$

Substituting the expression for G_{BS} into Equation 4.36 gives

$$\Big[(\epsilon s_{SS} - h_{SS}) - \underbrace{(\epsilon s_{SB} - h_{SB})\underbrace{(\epsilon s_{BB} - h_{BB})^{-1}}_{g_{BB}}(\epsilon s_{SB}^{\dagger} - h_{SB}^{\dagger})}_{\Sigma}\Big]G_{SS} = \mathbb{1} \tag{4.39}$$

it means that the Green's function of the surface region is obtanied as

$$G = \Big[\epsilon s_{SS} - u^{\dagger}\tilde{S}_{SS}^{-1/2}\tilde{H}_{SS}\tilde{S}_{SS}^{-1/2}u - \Sigma\Big]^{-1} \tag{4.40}$$

where $s_{SS} = \mathbb{1}$ and Σ is the self energy due to coupling to the bulk,

$$\Sigma = (\epsilon u^{\dagger}\tilde{S}_{SS}^{-1/2}\tilde{S}_{SB} - u^{\dagger}\tilde{S}_{SS}^{-1/2}\tilde{H}_{SB})\; g_{BB}\; (\epsilon\tilde{S}_{SB}^{\dagger}\tilde{S}_{SS}^{-1/2}u - \tilde{H}_{SB}^{\dagger}\tilde{S}_{SS}^{-1/2}u). \tag{4.41}$$

The calculation of the surface Green's function, g_{BB} is explained as for the Green's function of the semi-infinite reservoir, G in detail in Section 2.3. Then, the surface Green's function is calculated. The self energy can be acquired from the result of this calculation. The spectral function is calculated using this self energy.

4.3.2. Numerical Results for Realistic Structure

The study of passivation of the active species on the ZnS (111) surface has been carried out using periodic supercell models. In all cases, the constructed layer models are based on the ZnS (zinc blende) structure. The ZnS (111) facets are polar and should be passivated with ligands. Therefore, the interaction of the ligands with the ZnS (111) surface is considered. The oleic acid in the colloidal solution play a significant role of the capping ligand on the surface. We designed structures by removing the H atom in the carboxyl functional group of the oleic acid (OA) and binding it to the surface, and our ligand is now the oleate (OA^-) molecule. In this subsection, all possible configurations of the OA^- ligand on the ZnS (111) is considered.

We constructed models by different binding positions of the ligand (cis and trans OA^- molecule) on the ZnS (111) surface, which is Zn and S rich surfaces and by increasing the amount of capping ligands on the surface. All figures, the ligand on the surface is shown as: the carboxylate functional group of the oleate molecule, the COO^- group, is illustrated and R means the tail chain of the oleic acid. For the sake of simplicity, xy plane is shown with truncated tail chain of oleic acid. For realistic system, the spectral function and the time dependent occupancy are calculated as in the simplified model. The time dependent occupancy versus time graph is obtained by computing spectral functions of HOMO and LUMO levels for different binding configurations of OA^- molecule on ZnS (111) surface.

We note that the atomic arrangements of the surface lead to an expected distortion in the structure of the bare surface in the geometry optimization. First, cis-OA^- ligand on the Zn rich surface is considered. In Figure 4.9(a), the unrelaxed unit cell of cis-OA^- capping ligand on the Zn rich surface is shown where only one surface Zn atom is passivated with the cis-OA^- molecule. The relaxed unit cell is shown in Figure 4.9(b), we observe that both O atoms in the carboxylate group of oleate molecule bond to the surface Zn atoms. In Figure 4.9, the $3 \times 3 \times 1$ supercell is constructed from the relaxed unit cell (c) in z direction and (d) in the xy plane. Next, we calculate the spectral functions for frontier molecular orbitals of cis-OA^- molecule on the surface. For a free cis configuration of

oleic acid (OA) molecule, the HOMO value is 9.61 eV and the LUMO value is 9.99 eV. In Figure 4.9(e), HOMO and LUMO values for cis configuration of OA molecule represent purple and green color lines, respectively. Due to the interaction between the surface and cis-OA^- molecule, we can see discrepancy that the Lorenzian shapes are distorted as seen in Figure 4.9(e). We can also obverse that the shift increases on their bare energies and the broadening increases. The level spectra of the frontier molecules are symmetric as in the simplified model in Figures 4.2(c,g). The occupations for frontier molecules are obtained the same result because they have same spectral function behavior as shown in Figure 4.9(f). They continue to overlap with each other and decay to about 0.5 picoseconds. According to the Heisenberg uncertainty relations, the half life of each molecular level is calculated to be 0.04 picoseconds using the Equation 4.15 for the HOMO and the LUMO levels and the result is consistent with our calculation.

We continue the calculations of the spectral function and the time dependent occupancy using different configurations of the (111) facets capped by trans-OA^- molecules. Secondly, trans1-OA^- ligand on the Zn rich surface is considered. In Figure 4.10, (a) demonstrates the unrelaxed unit cell that each O atom in carboxylate functional group of trans1-OA^- bonds to one surface Zn atom, we see that the relaxed unit cell maintains this situation and has surface defects in (b), the $3 \times 3 \times 1$ supercell is constructed from the relaxed unit cell in z direction in (c) and in the xy plane in (d). We observe that passivation configurations for cis-OA^- and trans1-OA^- ligands on the Zn rich surface relax to the same binding position on the surface as seen Figure 4.9(d) and Figure 4.10(d). In the case of cis and trans configuration of the oleic acid, the tail chain of the oleic acid has no significant effect on the surface. Moreover, the interaction of trans2-OA^- ligand with the Zn rich surface is considered. In Figure 4.10, the unrelaxed unit cell is shown that each O atom in carboxylate functional group of trans2-OA^- bonds to two surface Zn atoms simultaneously in (e) and the surface of the relaxed unit cell is shown in (f) that one O atom bonds to one surface Zn atom and the other O atom bonds to two surface Zn atoms. Figure 4.10 illustrates the $3 \times 3 \times 1$ supercell of trans2-OA^- ligand on the ZnS surface in z direction in (g) and in the xy plane in (h). Although passivation configurations for trans1-OA^- and trans2-OA^- ligands on the Zn rich surface do not relax the same binding position on the surface, the results of the spectral functions of frontier molecular orbitals and their time dependent occupancies are same for these configurations as seen in Figure 4.10(i,j). For a free trans configuration of oleic acid (OA) molecule, the HOMO value is 9.63 eV and the LUMO value is 10.03 eV. Figure 4.10(i) demostrates that HOMO and LUMO values for trans configuration of OA molecule represent purple and green color lines, respectively.

We observe that the Lorentzian shapes are distorted due to the interaction between ligand and the surface. The spectra of the HOMO and the LUMO levels are shifted with increasing the broadening and the dressed states have narrow peaks. The level spectra have the same behavior as passivation configuration for cis-OA^- ligand on the surface as seen in Figure 4.9(e); however the spectrum of the HOMO shifts more from its bare state in Figure 4.10(i). These result in that their occupations have the same behavior with fluctuations during decay in Figure 4.10(j). We see that the occupations of passivation configurations for trans1-OA^- and trans2-OA^- ligands on the surface yield very similar results as the surface capped by cis-OA^- ligand can be seen in Figure 4.9(f) and Figure 4.10(j). The half life of the HOMO and the LUMO read again 0.04 picoseconds. For the cis-OA^-, trans1-OA^- and trans2-OA^- ligands on the Zn rich surface, we observe that the HOMO and the LUMO levels have the same behaviors as in the simplified model with the inter-level hopping $t' = 0$ where the hopping terms are identical values and the energy band gap is narrow and wider, and the occupations of these passivation configurations yield similar results as in the simplified in Figures 4.4(c,g).

Up to this part, we investigate the interaction between a single oleic acid and the Zn rich surface. We continue analyzing by increasing the amount of capping ligands on the surface. In Figure 4.11(a) and (b), the analysis for unrelaxed and relaxed unit cells shows that we observe that each trans3-OA^- ligands binds to two surface Zn atoms. Figure 4.11 shows that the $3 \times 3 \times 1$ supercell is constructed from two trans3-OA^- ligands per optimizated unitcell in z direction in (c) and in the xy plane in (d). In the case of two trans3-OA^- ligands per unit cell, we can clearly see that the Lorentzian widths overlap and their shapes are effectively distorted compared to passivation configurations of one ligand binding to the surface as shown in Figure 4.11(e). It is observed that the spectrum of the HOMO level has sharp peaks spreading around between 9 and 9.6 eV, the other spectrum of the LUMO level has sharp peaks spreading around between 9.6 and 10 eV. We can also see that their behavior significantly affects the time-dependent occupancy of HOMO and LUMO levels as shown in Figure 4.11(f). The time dependent occupancies of the states are obtained rapidly fluctuating during decay by difference oscillations of molecular levels. Additionally, the time dependent occupancy of the HOMO level has more oscillations than the LUMO level, because of having its Lorentzian peaks. The behavior of the HOMO and the LUMO levels due to the overlap shape resemble the simplified model with the inter-level hopping $t' = 0.20$ as Figure 4.3(g), where the hopping terms are identical values and the energy band gap is wider. The spectra behaviors are obtained fluctuations during decay with the different oscillation rates for this simplified model and

trans3-OA^- ligand in Figure 4.5(e) and Figure 4.11(f).

We have evaluated passivation configurations for the ligands on the Zn rich surface and, the calculations of the spectral function and the time dependent occupancy for different configurations. We now consider trans4-OA^- ligand on the S rich surface. Figure 4.12(a) demonstrates the unrelaxed structure of the unit cell of the trans4-OA^- ligand binding to two surface S atoms. The relaxed unit cell is shown as Figure 4.12(b) and we observe this ligand binds to the same Zn atom. The important point is that the (111) surface has rich S atom; however the O atoms in the carboxylate functional group of oleate molecule bond to the same Zn atom below the surface. Furthermore, another ligand on the S rich surface is trans5-OA^-. In Figure 4.13, (a) demostrates the unrelaxed unit cell of the trans5-OA^- ligand binding to the same surface S atom and the surface defects are formed in the relaxed unit cell as shown in (b). After the relaxation of the unit cell, the trans5-OA^- ligand bind to the Zn atom, such as the trans4-OA ligand. However, the trans5-OA^- ligand that only one O atom of its carboxylate functional group bonds to one Zn atom binds differently to the surface than the trans4-OA^- ligand. In Figure 4.12 and Figure 4.13, the $3 \times 3 \times 1$ supercell is constructed from the relaxed unit cell of trans4-OA^- and trans5-OA^- ligands on the S rich surface in z direction in (c) and in the xy plane in (d), respectively. For the spectrum of the HOMO and the LUMO levels, Lorentzian shapes are distorted, the shift and the broadening increases as seen in Figure 4.12(e) and Figure 4.13(e). However, the spectra of trans5-OA^- ligand on the surface overlap slightly more than trans4-OA^- ligand on the surface. In the time dependent occupancies of the molecular levels, the fluctuactions overlap completely during decay as seen in Figure 4.12(f) and Figure 4.13(f). Both of the Lorentzian widths of the frontier molecular orbitals read 0.05 eV , and the same result is observed with comparing to the Lorentzian widths of ligands on the Zn rich surface without two ligands on the surface per unit cell. The half life is measured to be 0.04 picoseconds for each occupation of the molecular levels. According to the Heisenberg uncertainty relations, the half life are found to consistent with the predicted values for realistic models.

We consider two ligands on the ZnS (111) surface for the S rich atoms per unit cell. Figure 4.14(a) shows that the unrelaxed unit cell is two trans6-OA^- ligands on the S rich surface. The relaxed unit cell is shown in Figure 4.14(b). We observe that surface defects are formed while Zn atoms relax by aligning them with S atoms and each trans6-OA^- ligand binds to one Zn atom on the surface. In Figure 4.14, the $3 \times 3 \times 1$ supercell is constructed from two trans6-OA^- ligands on the S rich surface per unit cell as shown in z direction in (c) and in the xy plane in (d). We can see that the Lorentzians overlap and

their shapes are significantly distorted as seen in Figure 4.14(e). For the S rich surface, the shift and the broadening of the spectral functions on molecular levels for trans6-OA^- ligand on the surface spread around between 9 and 10 eV with having lots of peaks when compared to that the first two ligands as trans4-OA^- and trans5-OA^-. The spectrum of LUMO distinctly has two peaks, and the spectrum of HOMO has several peaks. These behaviors result in the oscillations during decay as illustrated in Figure 4.14(f). The spectrum of LUMO decays faster than the spectrum of the HOMO due to having the different Lorentzian widths of them. The behavior of the level spectra is similar composed to the simplified model with the inter-level hopping $t' = 0.20$ as Figure 4.3(e), where the hopping terms are identical values and the energy band gap is narrow. For the time dependent occupancy of molecular levels of this simplified model and two trans6-OA^- ligands per unit cell, the fluctuations during decay have the similar behaviors as in Figure 4.5(e) and Figure 4.14(f).

To sum up, the passivation configurations are relaxed by binding between OA^- ligand and the Zn atom on the ZnS (111) surface, even if the atoms on the surface are Zn or S atoms. In the Zn and S rich surfaces, the dressed states for the trans and cis configurations of oleic acid ligand on the surface have a narrowing the Lorentzian widths. Besides, we have observed that the Lorentzians overlap and their shapes are extremely distorted for the spectral function on frontier molecular orbitals for two trans-OA^- ligand on the Zn and S rich surfaces per unit cell. We have investigated that their spectra behavior affects on their time dependent occupancies. Additionally, we compared our passivation configurations with a simplified model showing the same spectra behavior. For one ligand binding to the surface, the Lorentzian width read in the Figures and the half life is calculated using the uncertainty relations. Afterwards, we acquired that the measured value of the half life from the time dependent occupancy is consistent with the predicted value from the uncertainty relations.

In order to analyze the interaction between different configurations of oleate molecule binding to the ZnS (111) surface, the binding energies are determined by

$$E_{bind} = E_{tot} - E_{surf} - E_{lig} \tag{4.42}$$

where E_{tot} is the total energy of the optimized structure with the ZnS surface-bound oleate ligands per unit cell, E_{surf} is the energy of the relaxed ZnS (111) surface without any capping ligand per unit cell and E_{lig} is the energy of the free oleate molecule. In the surface with terminated Zn layer, the binding energies of the surface-capping ligands

for cis-OA^-, trans1-OA^-, trans2-OA^- and trans3-OA^- are calculated -7.25 eV, -7.28 eV, -7.05 eV and -6.31 eV, respectively. In the surface with terminated S layer, the binding energies of the surface-capping ligands for trans4-OA^-, trans5-OA^- and trans6-OA^- are calculated -2.38 eV, -1.36 eV and -1.49 eV, respectively. The binding energies of different configurations are calculated accordingly to the Equation 4.42 as shown in Table 4.2, where the binding energy of the surface-bound ligands (trans3-OA^- and trans6-OA^-) is written for two oleate molecules.

Table 4.2. The binding energies of the capping ligands.

ZnS (111) surface with terminated Zn layer	
Passivation	The binding energy (eV) per unit cell
cis - OA^-	-7.25
trans1 - OA^-	-7.28
trans2 - OA^-	-7.05
trans3 - OA^-	-12.62*
ZnS (111) surface with terminated S layer	
Passivation	The binding energy (eV) per unit cell
trans4 - OA^-	-2.38
trans5 - OA^-	-1.36
trans6 - OA^-	-2.97*

* The binding energy is for two oleate ligands.

Both observations indicate that oxygen atom, which is in the carboxylate group of oleate, binds to the Zn atoms on the surface. Hence, in realistic models, the ligand binding energy on S rich surface is much smaller than that on Zn rich surface. In all possible binding configurations, trans1-OA^- bind more strongly to the surface than other ligands. Additionally, trans1-OA^- ligand binding energies on Zn rich surface are consistent with the experimental value of -7.52 eV cohesive energy for ZnO as a semiconductor [62].

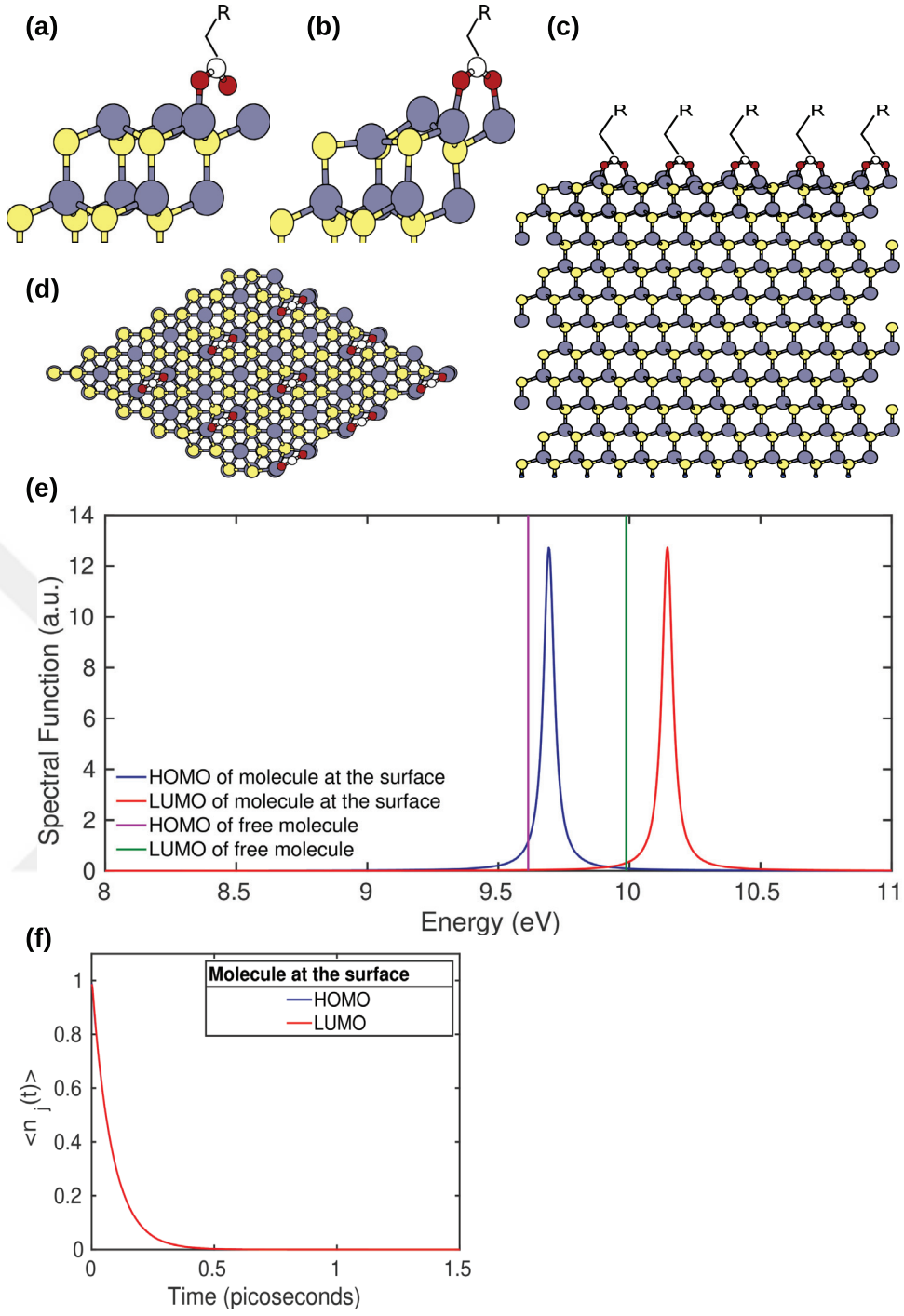

Figure 4.9. ZnS (111) surface capped by cis-OA$^-$ molecule. (a) Unrelaxed and (b) relaxed unit cell in side-view. (c) $3 \times 3 \times 1$ supercell from the relaxed unit cell in side-view. (d) The supercell with truncated tail chains in top-view. (e) Spectral function of the HOMO and the LUMO. (f) The time dependent occupancy of the HOMO and the LUMO.

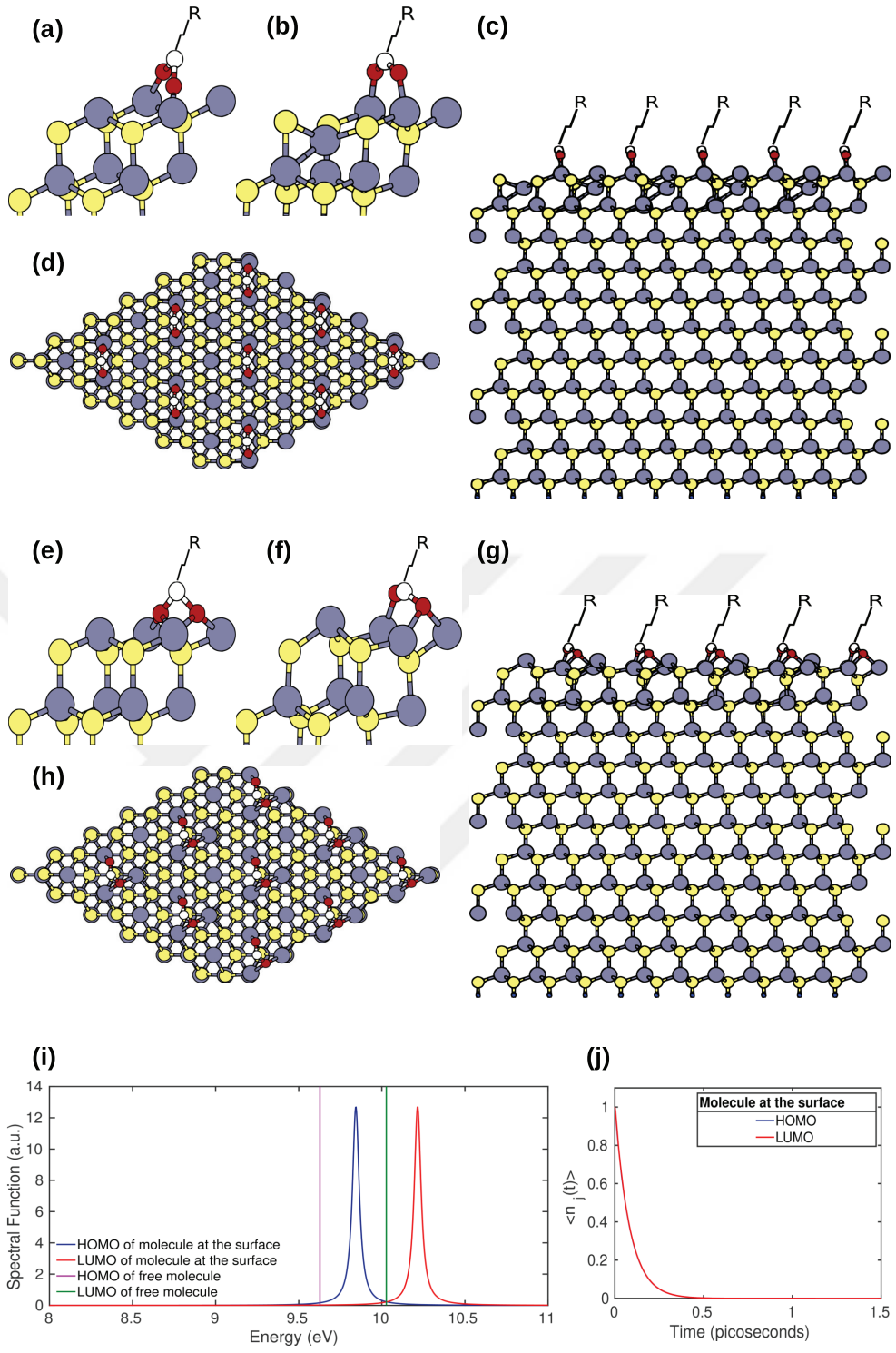

Figure 4.10. (a,b,c,d) and (e,f,g,h) for ZnS (111) surface capped by trans1-OA$^-$ and trans2-OA$^-$ molecules, respectively. (a,e) Unrelaxed and (b,f) relaxed unit cell in side-view. (c,g) $3 \times 3 \times 1$ supercell from the relaxed unit cell in side-view. (d,h) The supercell with truncated tail chains in top-view. (i) Spectral function of the HOMO and the LUMO. (j) The time dependent occupancy of the HOMO and the LUMO.

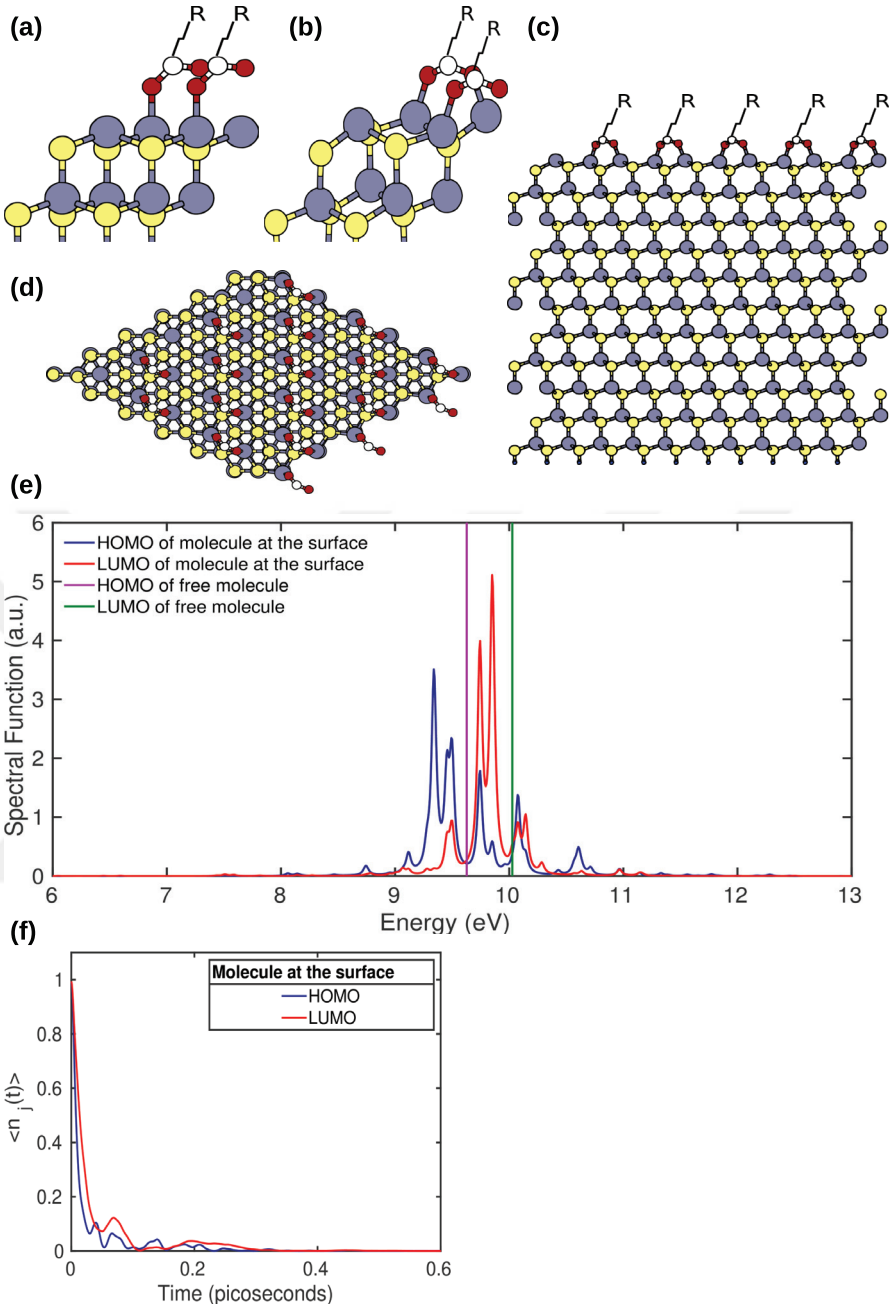

Figure 4.11. ZnS (111) surface capped by trans3-OA$^-$ molecule. (a) Unrelaxed and (b) relaxed unit cell in side-view. (c) $3 \times 3 \times 1$ supercell from the relaxed unit cell in side-view. (d) The supercell with truncated tail chains in top-view. (e) Spectral function of the HOMO and the LUMO. (f) The time dependent occupancy of the HOMO and the LUMO.

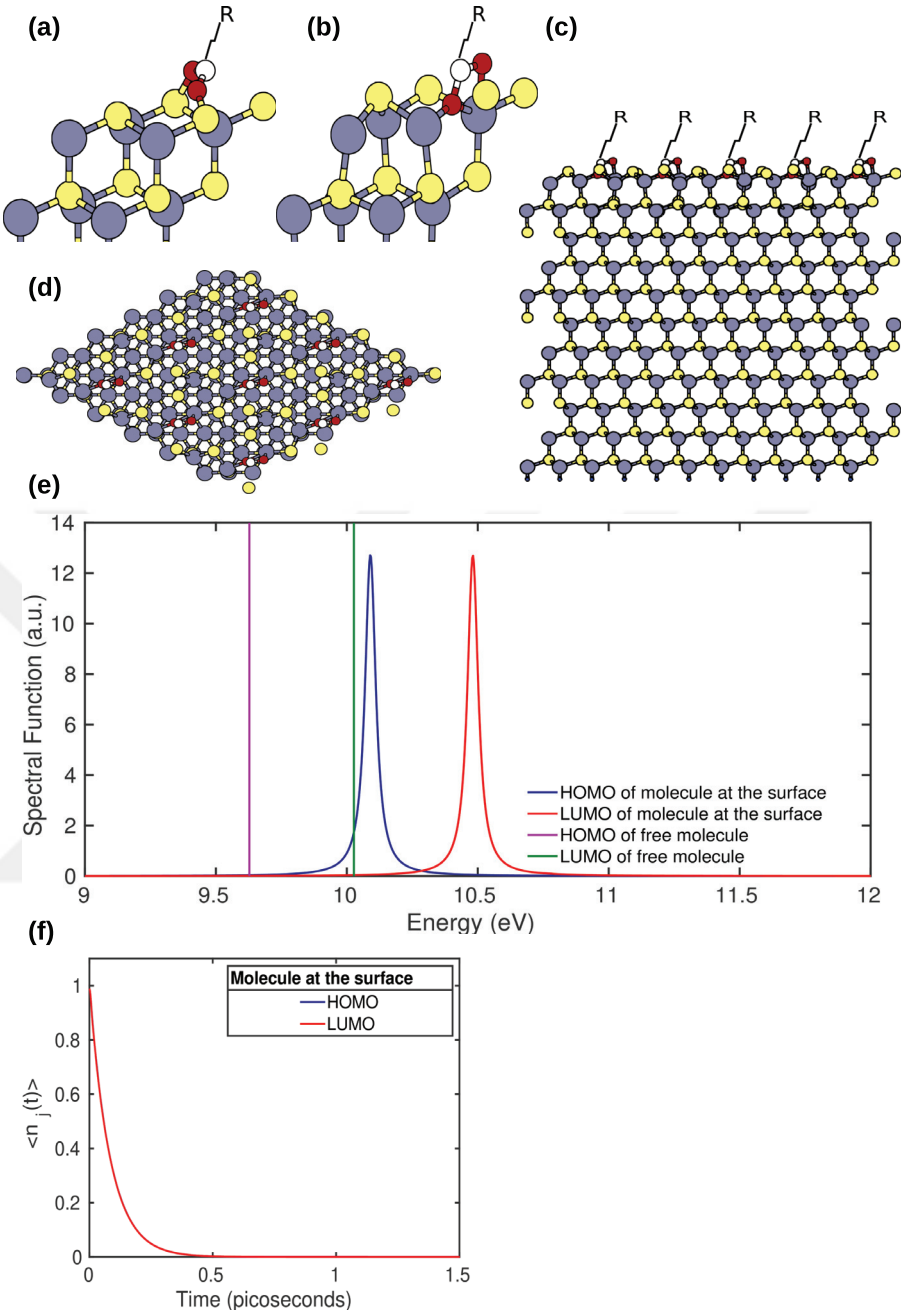

Figure 4.12. ZnS (111) surface capped by trans4-OA$^-$ molecule. (a) Unrelaxed and (b) relaxed unit cell in side-view. (c) $3 \times 3 \times 1$ supercell from the relaxed unit cell in side-view. (d) The supercell with truncated tail chains in top-view. (e) Spectral function of the HOMO and the LUMO. (f) The time dependent occupancy of the HOMO and the LUMO.

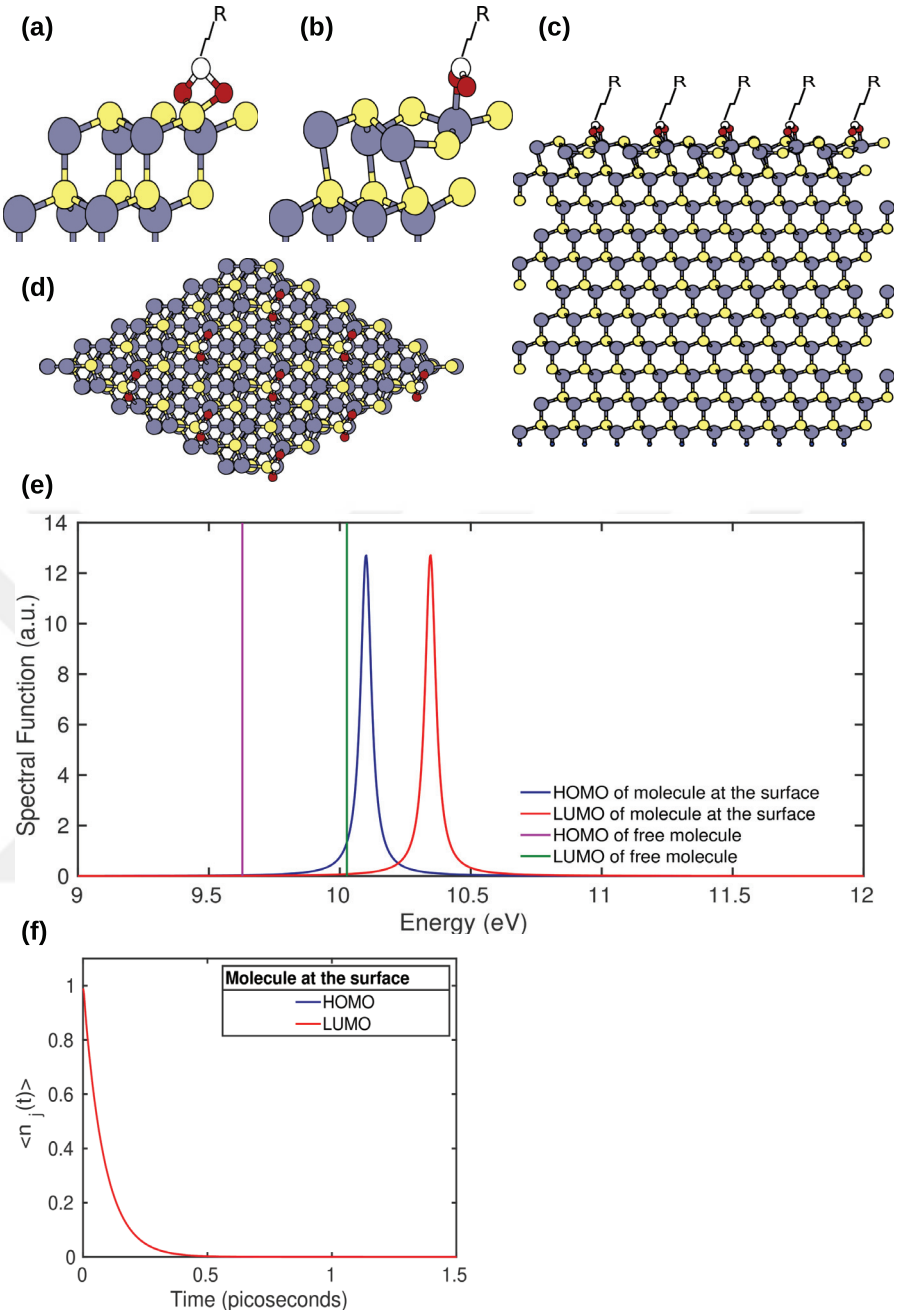

Figure 4.13. ZnS (111) surface capped by trans5-OA$^-$ molecule. (a) Unrelaxed and (b) relaxed unit cell in side-view. (c) $3 \times 3 \times 1$ supercell from the relaxed unit cell in side-view. (d) The supercell with truncated tail chains in top-view. (e) Spectral function of the HOMO and the LUMO. (f) The time dependent occupancy of the HOMO and the LUMO.

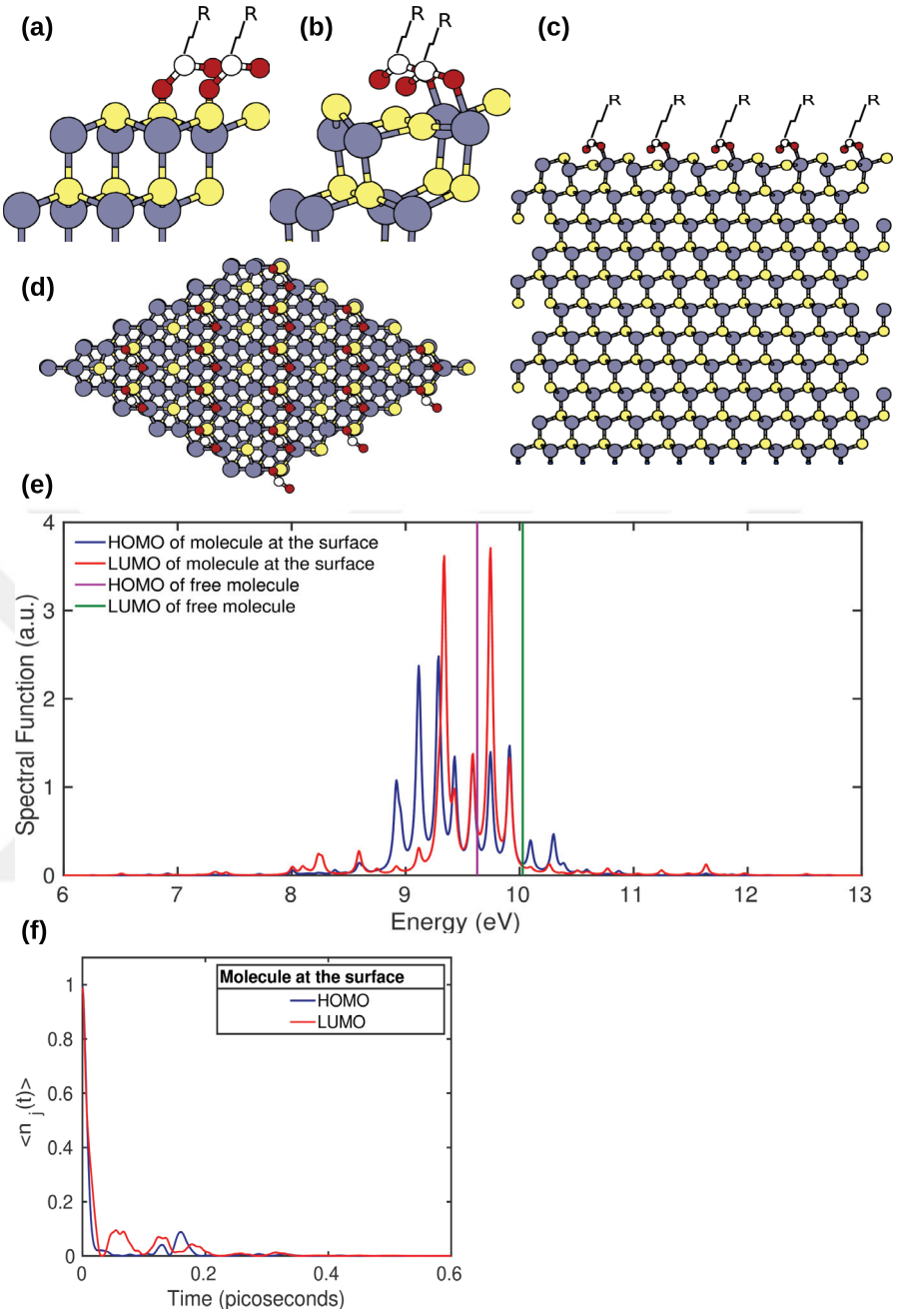

Figure 4.14. ZnS (111) surface capped by trans6-OA^{-} molecule. (a) Unrelaxed and (b) relaxed unit cell in side-view. (c) $3 \times 3 \times 1$ supercell from the relaxed unit cell in side-view. (d) The supercell with truncated tail chains in top-view. (e) Spectral function of the HOMO and the LUMO. (f) The time dependent occupancy of the HOMO and the LUMO.

CHAPTER 5

CONCLUSION

In this thesis, we have investigated the excitation dynamics on semiconductor surfaces, which are passivated with organic molecules for different molecular configurations by modeling them using density functional theory based tight binding (DFTB).

The simplified model was constructed to better understand the excitation dynamics on the surface by calculating time dependent occupations of frontier molecular orbitals for two different cases with interacting and non-interacting between the highest occupied and the lowest unoccupied molecular orbitals (HOMO and LUMO). In order to explain the time dependent occupations, we have investigated the behaviors of the spectral functions.

In the simplified model, we investigate the effects of coupling strength and inter-level spacing on the shape and widths of the spectral functions. The obvious effect of the interaction is to shift and broaden the HOMO and LUMO levels. When the broadening is small compared to inter-level spacing, the spectral functions of the dressed states do not overlap appreciably, hence they do not affect each other and each level's decay rate is determined with its coupling strength to the reservoir. On the other hand, when the broadening is comparable with the inter-level spacing the dressed states' spectra start to overlap and they indirectly affect each other. Antiresonance line shape is observed at the energy where the neighboring states' spectrum has a maximum. When the spectral width exceeds the inter-level spacing, the effect is even more pronounced and the spectral shape is strongly disturbed so that the Lorentzian shape is almost lost. Accordingly, one observes oscillatory decay in the time dependent occupations of the molecular levels. Once a coupling term is introduced between the molecular levels, the dressed states contain two peaks from both of the bare states. Hence the time dependent occupation displays stronger and periodic oscillations during decay.

For the realistic system, the spectral function and the time dependent occupancy are calculated based on the same formulation. We have designed different binding positions for ZnS (111) surface such as Zn atoms and S atoms rich surfaces passivated with oleic acid (OA) molecule. We have constructed the realistic models that cis-OA^-, trans1-OA^- trans2-$OA^-$and trans3-OA^- molecules are bound to Zn rich surfaces and then trans4-OA^-, trans5-$OA^-$and trans6-OA^- are bound to S rich surfaces. First, cis and trans configuration of oleic acid are bound to Zn rich surfaces and similar spectral function

behaviors are obtained using cis-OA^-, trans1-OA^- and trans2-OA^- molecules, as their optimized structures are relaxed with the same configurations. For S rich surface, the spectra of trans4-OA^- and trans5-OA^- molecules binding the surface have very similar behaviors, but the spectra overlap very little for surface passivated with trans5-OA^- molecule. Their occupations continue to overlap with each other. Next, we have increased the amount of ligands on the surface as two oleate molecules in the unit cell. Consequently, Lorentztian widths overlap and their shapes are deformed more effectively for trans3-OA^- and trans6-OA^- molecules bound to Zn and S rich surfaces, respectively. This behavior dramatically affects the time dependent occupancy of the HOMO and the LUMO where the fluctuations increase more rapidly. The half life is quantified from the Lorentzian width and it is found to be consistent with the predicted values by the uncertainty relations for the simplified and realistic models. Moreover, we have obtained that oxygen atoms in the carboxylate group of oleate are bonded to Zn atoms even if there are S atoms on the surface. Secondly, the binding energies of different coverage ratios of surfaces are calculated. The binding energies of the Zn rich surface bound capping ligands are consistent with experimental results, where trans1-OA^- bind more strongly to the surface than other ligands.

In addition to these studies, the energy band gap for the quaternary $Zn_{1-x}Cd_xS_{1-y}Se_y$ nanoalloys are calculated. The lattice parameters of ternary and quaternary bulk nanoalloys are obtained by linear interpolation. X-Ray diffraction spectra of some nanoalloys have also been investigated.

REFERENCES

[1] Feynman, R. P. There's plenty of room at the bottom [data storage]. *Journal of microelectromechanical systems* **1992**, *1*, 60–66.

[2] Peng, X.; Manna, L.; Yang, W.; Wickham, J.; Scher, E.; Kadavanich, A.; Alivisatos, A. P. Shape control of CdSe nanocrystals. *Nature* **2000**, *404*, 59.

[3] Manna, L.; Milliron, D. J.; Meisel, A.; Scher, E. C.; Alivisatos, A. P. Controlled growth of tetrapod-branched inorganic nanocrystals. *Nature materials* **2003**, *2*, 382.

[4] Henglein, A. Small-particle research: physicochemical properties of extremely small colloidal metal and semiconductor particles. *Chemical reviews* **1989**, *89*, 1861–1873.

[5] Trindade, T.; O'Brien, P.; Pickett, N. L. Nanocrystalline semiconductors: synthesis, properties, and perspectives. *Chemistry of Materials* **2001**, *13*, 3843–3858.

[6] Kuchibhatla, S. V.; Karakoti, A.; Bera, D.; Seal, S. One dimensional nanostructured materials. *Progress in materials science* **2007**, *52*, 699–913.

[7] Bera, D.; Kuiry, S. C.; Seal, S. Synthesis of nanostructured materials using template-assisted electrodeposition. *Jom* **2004**, *56*, 49–53.

[8] Frecker, T.; Bailey, D.; Arzeta-Ferrer, X.; McBride, J.; Rosenthal, S. J. Quantum dots and their application in lighting, displays, and biology. *ECS Journal of Solid State Science and Technology* **2016**, *5*, R3019–R3031.

[9] Jiang, Y.; Cho, S.-Y.; Shim, M. Light-emitting diodes of colloidal quantum dots and nanorod heterostructures for future emissive displays. *Journal of Materials Chemistry C* **2018**, *6*, 2618–2634.

[10] Hetsch, F.; Zhao, N.; Kershaw, S. V.; Rogach, A. L. Quantum dot field effect transistors. *Materials Today* **2013**, *16*, 312–325.

[11] Prasad, S.; AlHesseny, H.; AlSalhi, M.; Devaraj, D.; Masilamai, V. A high power, frequency tunable colloidal quantum dot (CdSe/ZnS) laser. *Nanomaterials* **2017**, *7*, 29.

[12] Gao, X.; Cui, Y.; Levenson, R. M.; Chung, L. W.; Nie, S. In vivo cancer targeting and imaging with semiconductor quantum dots. *Nature biotechnology* **2004**, *22*, 969.

[13] Bukowski, T. J.; Simmons, J. H. Quantum dot research: current state and future prospects. *Critical Reviews in Solid State and Material Sciences* **2002**, *27*, 119–142.

[14] Choi, A. O.; Maysinger, D. *Semiconductor Nanocrystal Quantum Dots*; Springer, 2008; pp 349–365.

[15] Tartakovskii, A. *Quantum dots: optics, electron transport and future applications*; Cambridge University Press, 2012.

[16] Bruchez, M.; Moronne, M.; Gin, P.; Weiss, S.; Alivisatos, A. P. Semiconductor nanocrystals as fluorescent biological labels. *science* **1998**, *281*, 2013–2016.

[17] Bera, D.; Qian, L.; Holloway, P. H. 19 Semiconducting Quantum Dots for Bioimaging. *Drug Delivery Nanoparticles Formulation and Characterization* **2016**, *191*, 349.

[18] Chan, W. C.; Maxwell, D. J.; Gao, X.; Bailey, R. E.; Han, M.; Nie, S. Luminescent quantum dots for multiplexed biological detection and imaging. *Current opinion in biotechnology* **2002**, *13*, 40–46.

[19] Dingle, R.; Wiegmann, W.; Henry, C. H. Quantum States of Confined Carriers in Very Thin AlxGa1-x As-GaAs-AlxGa1-xAs Heterostructures. *Physical Review Letters* **1974**, *33*, 827.

[20] Wu, S.; Cheng, L.; Wang, Q. Excitonic effects and related properties in semiconductor nanostructures: roles of size and dimensionality. *Materials Research Express* **2017**, *4*, 085017.

[21] Davies, J. H. *The physics of low-dimensional semiconductors: an introduction*; Cambridge university press, 1998.

[22] Wang, Y.; Herron, N. Nanometer-sized semiconductor clusters: materials synthesis, quantum size effects, and photophysical properties. *The Journal of Physical Chemistry* **1991**, *95*, 525–532.

[23] Bang, J.; Yang, H.; Holloway, P. H. Enhanced and stable green emission of ZnO nanoparticles by surface segregation of Mg. *Nanotechnology* **2006**, *17*, 973–978.

[24] Kucur, E.; Bücking, W.; Giernoth, R.; Nann, T. Determination of defect states in semiconductor nanocrystals by cyclic voltammetry. *The Journal of Physical Chemistry B* **2005**, *109*, 20355–20360.

[25] Bera, D.; Qian, L.; Tseng, T.-K.; Holloway, P. H. Quantum dots and their multimodal applications: a review. *Materials* **2010**, *3*, 2260–2345.

[26] Dzhagan, V.; Lokteva, I.; Himcinschi, C.; Jin, X.; Kolny-Olesiak, J.; Zahn, D. R. Phonon Raman spectra of colloidal CdTe nanocrystals: effect of size, non-stoichiometry and ligand exchange. *Nanoscale research letters* **2011**, *6*, 79.

[27] Chen, X.; Samia, A. C.; Lou, Y.; Burda, C. Investigation of the crystallization process in 2 nm CdSe quantum dots. *Journal of the American Chemical Society* **2005**, *127*, 4372–4375.

[28] Navarro, D. A.; Banerjee, S.; Aga, D. S.; Watson, D. F. Partitioning of hydrophobic CdSe quantum dots into aqueous dispersions of humic substances: Influence of capping-group functionality on the phase-transfer mechanism. *Journal of colloid and interface science* **2010**, *348*, 119–128.

[29] Regulacio, M. D.; Han, M.-Y. Composition-tunable alloyed semiconductor nanocrystals. *Accounts of chemical research* **2010**, *43*, 621–630.

[30] Owen, J. The coordination chemistry of nanocrystal surfaces. *Science* **2015**, *347*, 615–616.

[31] Colvin, V.; Goldstein, A.; Alivisatos, A. Semiconductor nanocrystals covalently bound to metal surfaces with self-assembled monolayers. *Journal of the American Chemical Society* **1992**, *114*, 5221–5230.

[32] Murray, C.; Kagan, C.; Bawendi, M. Self-organization of CdSe nanocrystallites into three-dimensional quantum dot superlattices. *Science* **1995**, *270*, 1335–1338.

[33] Knowles, K. E.; Frederick, M. T.; Tice, D. B.; Morris-Cohen, A. J.; Weiss, E. A. Colloidal quantum dots: think outside the (particle-in-a-) box. *The Journal of Physical Chemistry Letters* **2011**, *3*, 18–26.

[34] Yang, P.; Tretiak, S.; Ivanov, S. Influence of surfactants and charges on CdSe quantum dots. *Journal of Cluster Science* **2011**, *22*, 405.

[35] Drijvers, E.; De Roo, J.; Martins, J. C.; Infante, I.; Hens, Z. Ligand displacement exposes binding site heterogeneity on CdSe nanocrystal surfaces. *Chemistry of Materials* **2018**, *30*, 1178–1186.

[36] Van Der Stam, W.; Rabouw, F. T.; Vonk, S. J.; Geuchies, J. J.; Ligthart, H.; Petukhov, A. V.; de Mello Donega, C. Oleic acid-induced atomic alignment of ZnS polyhedral nanocrystals. *Nano letters* **2016**, *16*, 2608–2614.

[37] Chen, S.; Liu, W. Oleic acid capped PbS nanoparticles: synthesis, characterization and tribological properties. *Materials Chemistry and Physics* **2006**, *98*, 183–189.

[38] dos Santos, J. A. L.; Baum, F.; Kohlrausch, E. C.; Tavares, F. C.; Pretto, T.; dos Santos, F. P.; Leite Santos, J. F.; Khan, S.; Leite Santos, M. J. 3-Mercaptopropionic, 4-Mercaptobenzoic, and Oleic Acid-Capped CdSe Quantum Dots: Interparticle Distance, Anchoring Groups, and Surface Passivation. *Journal of Nanomaterials* **2019**, *2019*.

[39] Luan, W.; Yang, H.; Fan, N.; Tu, S.-T. Synthesis of efficiently green luminescent CdSe/ZnS nanocrystals via microfluidic reaction. *Nanoscale Research Letters* **2008**, *3*, 134.

[40] Sevim, S.; Memisoglu, G.; Varlikli, C.; Doğan, L. E.; Tascioglu, D.; Ozcelik, S. An ultraviolet photodetector with an active layer composed of solution processed polyfluorene: Zn0. 71Cd0. 29S hybrid nanomaterials. *Applied Surface Science* **2014**, *305*, 227–234.

[41] Born, M.; Oppenheimer, R. Zur quantentheorie der molekeln. *Annalen der Physik*

1927, *389*, 457–484.

[42] Hartree, D. R. The wave mechanics of an atom with a non-coulomb central field. Part II. Some results and discussion. Mathematical Proceedings of the Cambridge Philosophical Society. 1928; pp 111–132.

[43] Fock, V. Näherungsmethode zur Lösung des quantenmechanischen Mehrkörperproblems. *Zeitschrift für Physik* **1930**, *61*, 126–148.

[44] Slater, J. C. A simplification of the Hartree-Fock method. *Physical review* **1951**, *81*, 385.

[45] Kohn, W.; Sham, L. J. Self-consistent equations including exchange and correlation effects. *Physical review* **1965**, *140*, A1133.

[46] Hohenberg, P.; Kohn, W. Inhomogeneous electron gas. *Physical review* **1964**, *136*, B864.

[47] Martin, R. M.; Martin, R. M. *Electronic structure: basic theory and practical methods*; Cambridge university press, 2004.

[48] Jones, R. O.; Gunnarsson, O. The density functional formalism, its applications and prospects. *Reviews of Modern Physics* **1989**, *61*, 689.

[49] Perdew, J. P.; Burke, K.; Ernzerhof, M. Generalized gradient approximation made simple. *Physical review letters* **1996**, *77*, 3865.

[50] Slater, J. C.; Koster, G. F. Simplified LCAO method for the periodic potential problem. *Physical Review* **1954**, *94*, 1498.

[51] Goringe, C.; Bowler, D.; Hernandez, E. Tight-binding modelling of materials. *Reports on Progress in Physics* **1997**, *60*, 1447.

[52] Froyen, S.; Harrison, W. A. Elementary prediction of linear combination of atomic orbitals matrix elements. *Physical Review B* **1979**, *20*, 2420.

[53] Chadi, D. Atomic and electronic structures of reconstructed Si (100) surfaces. *Physical*

Review Letters **1979**, *43*, 43.

[54] Seifert, G.; Joswig, J.-O. Density-functional tight binding—An approximate density-functional theory method. *Wiley Interdisciplinary Reviews: Computational Molecular Science* **2012**, *2*, 456–465.

[55] Elstner, M.; Porezag, D.; Jungnickel, G.; Elsner, J.; Haugk, M.; Frauenheim, T.; Suhai, S.; Seifert, G. Self-consistent-charge density-functional tight-binding method for simulations of complex materials properties. *Physical Review B* **1998**, *58*, 7260.

[56] Sancho, M. L.; Sancho, J. L.; Rubio, J. Quick iterative scheme for the calculation of transfer matrices: application to Mo (100). *Journal of Physics F: Metal Physics* **1984**, *14*, 1205.

[57] Nardelli, M. B. Electronic transport in extended systems: Application to carbon nanotubes. *Physical Review B* **1999**, *60*, 7828.

[58] Anderson, P. W. Localized Magnetic States in Metals. *Phys. Rev.* **1961**, *124*, 41–53.

[59] Fano, U. Effects of configuration interaction on intensities and phase shifts. *Physical Review* **1961**, *124*, 1866.

[60] Mahan, G. D. *Many-Particle Physics (Physics of Solids and Liquids)*; Springer, 2000.

[61] Müller, W.; Schiller, R.; Nolting, W. Understanding of surface states in a correlated electron system. *The European Physical Journal B-Condensed Matter and Complex Systems* **2000**, *16*, 705–718.

[62] Özgür, Ü.; Alivov, Y. I.; Liu, C.; Teke, A.; Reshchikov, M.; Doğan, S.; Avrutin, V.; Cho, S.-J.; Morkoç,; H, A comprehensive review of ZnO materials and devices. *Journal of applied physics* **2005**, *98*, 11.

APPENDIX A

DETERMINATION OF SURFACE LAYER SIZE

In experiments, quantum dots are much larger as compared to the clusters in theoretical study. In order to obtain correspondence, the results of XRD patterns of $(2 \times 2 \times 2)$ bulk materials ($Zn_{0.50}Cd_{0.50}S_{0.75}Se_{0.25}$, $Zn_{0.50}Cd_{0.50}$ $S_{0.50}Se_{0.50}$, $Zn_{0.25}Cd_{0.75}S_{0.50}Se_{0.50}$) are compared with experimental measurements of quantum dots and the results are consonant with each other. Thus, it is decided to use bulk materials instead of quantum dots. The size of the supercell is small for this approach, we need to increase the number of atoms in the supercell in order to defect how many neighbouring atoms are enough for the simulation. The construction of the supercell starts with the primitive unit cell ZnS. In the following Figure A.1, we can see this constructed ZnS supercell $(6 \times 6 \times 6)$ containing 216 S and 216 Zn atoms.

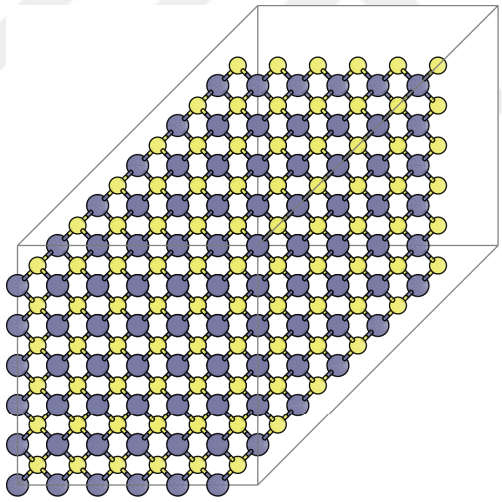

Figure A.1. Supercell $6 \times 6 \times 6$ from the primitive unit cell of ZnS. The gray and yellow balls stand for Zn and S atoms, respectively.

All matrix elements of this supercell are calculated by using the DFTB method. Beginning with the calculation of overlap matrix, the interaction between neighbouring orbitals are found. The supercell consists two different species, where S atom consists a $3s$ and three $3p$ valence orbitals and Zn atom consists a $4s$ and five $3d$ valence orbitals. In addition to this, three $3p$ are included in the calculation of overlap for Zn atom. The

overlap integral S values are calculated for s, p and d atomic orbitals. The overlap matrix is a square matrix and it is always symmetric. ZnS supercell has the overlap matrix with 2808 x 2808 dimensions.

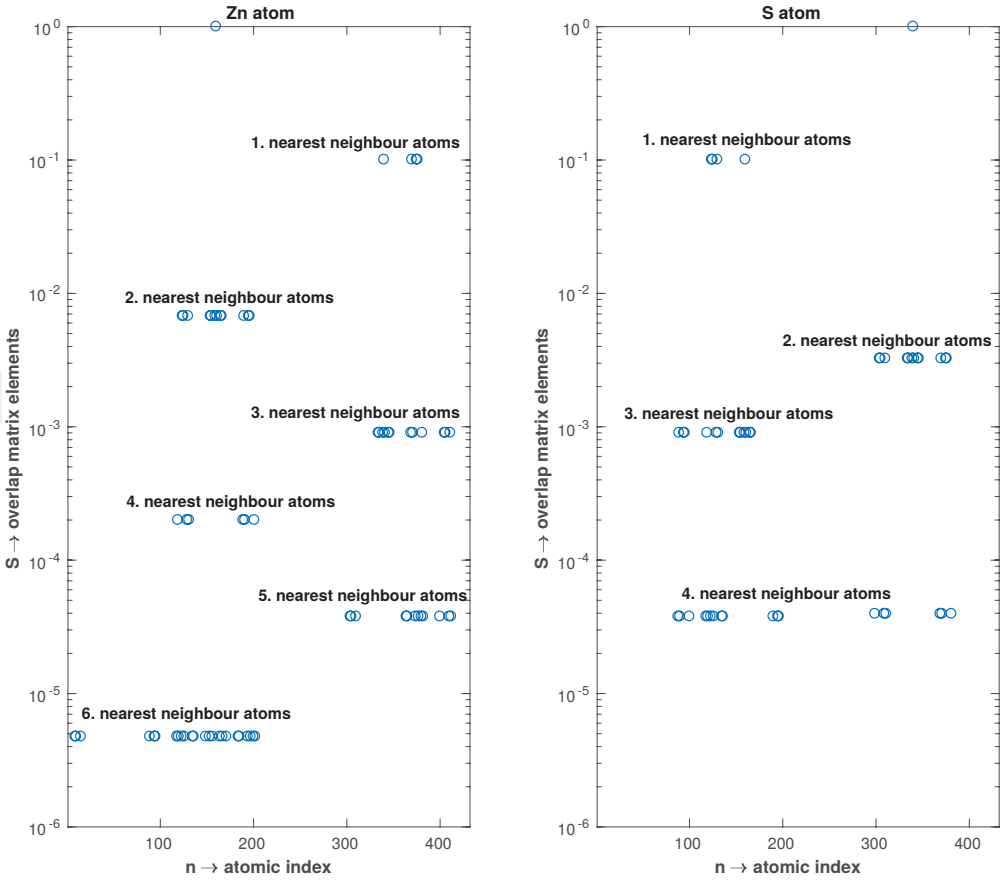

Figure A.2. Magnitude of the elements of overlap matrix for nearest-neigbour overlap only. 160. Zn atom and 340. S atom are selected from supercell.

In Figure A.2, the overlap values are shown where the matrix element of each atom is taken its maximum absolute value. An atom which is Zn atom or S atom in ZnS supercell can be selected random atomic index for calculation of overlap matrix, because it has same result for all Zn or S atoms. Also, we can calculate the distance between atoms, so S and Zn atoms are chosen from in the center of the supercell. We can select 160. Zn atom and 340. S atom in the center of the supercell. The calculation of overlap matrix and distances between atoms in supercell are done with these selected Zn and S atoms. Then, distances can be determined between each atom in the supercell for 160. Zn atom and 340. S atom, which is demonstrated in Figure A.3. Detailed information about Figure A.3, distances of Zn and S atoms with nearest neighbour atoms are given in Table

A.1. Figure A.2 investigates only nearest neigbour atoms and checking number of atoms at nearest neighbour levels from Figure A.3, and consequently there are 6 and 4 nearest neighbour for Zn and S atoms, respectively. After these calculations, we can obtain that fourth nearest neighbour atoms can be enough for constructing Hamiltonian for a ZnS cluster. However, we can decide to design the surface structure of ZnS by sixth nearest neighbour atoms, because the computational cost will not change dramatically.

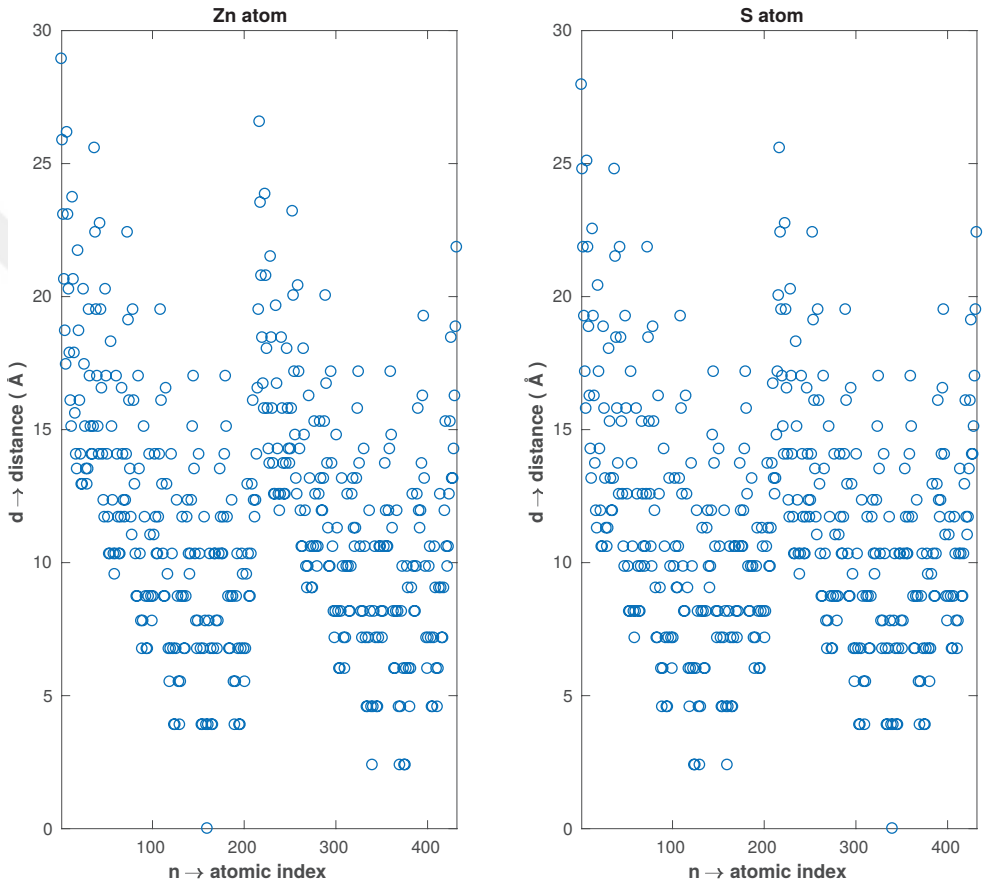

Figure A.3. From left to right, distance between 160. Zn atom and each atom, 340. S atom and each atom in ZnS supercell.

Table A.1. Number of atoms, distances between atoms (in Å) and kind of bond at nearest neighbour levels, for 160. Zn atom and 340. S atom in ZnS supercell.

Zn atom			
Nearest neighbours	Number of atoms	Distance between atoms (Å)	Kind of bond
1	4	2.3891	Zn-S
2	12	3.9013	Zn-Zn
3	12	4.5747	Zn-S
4	6	5.5173	Zn-Zn
5	12	6.0124	Zn-S
6	21*	6.7573	Zn-Zn
S atom			
1	4	2.3891	S-Zn
2	12	3.9013	S-S
3	12	4.5747	S-Zn
4	6	5.5173	S-S
5	12	6.0124	S-Zn

* In Figure A.2, the sixth nearest neighbour has 24 atoms.